Intracluster magnetic filaments and an encounter with a radio jet

Rudnick, L.; Brüggen, M.; Brunetti, G.; Cotton, W.D.; Forman, W.; Jones, T.W.; ... ; Weeren, R. J. van

Note: To cite this publication please use the final published version (if applicable).

Intracluster Magnetic Filaments and an Encounter with a Radio Jet

L. Rudnick[1] ⓘ, M. Brüggen[2] ⓘ, G. Brunetti[3] ⓘ, W. D. Cotton[4] ⓘ, W. Forman[5] ⓘ, T. W. Jones[1] ⓘ, C. Nolting[6] ⓘ,
G. Schellenberger[5] ⓘ, and R. van Weeren[7] ⓘ

[1] Minnesota Institute for Astrophysics, University of Minnesota, 116 Church St. SE, Minneapolis, MN 55455, USA; larry@umn.edu
[2] University of Hamburg, Gojenbergsweg 112, D-21029 Hamburg, Germany
[3] INAF—Istituto di Radioastronomia, Via P. Gobetti 101, I-40129 Italy
[4] National Radio Astronomy Observatory, 520 Edgemont Road, Charlottesville, VA 22903 USA
[5] Center for Astrophysics | Harvard & Smithsonian, 60 Garden Street, Cambridge, MA 02138, USA
[6] Department of Physics and Astronomy, College of Charleston, 66 George Street, Charleston, SC 29424, USA
[7] Leiden Observatory, Leiden University, PO Box 9513, 2300 RA Leiden, The Netherlands
Received 2022 May 16; revised 2022 June 24; accepted 2022 June 28; published 2022 August 24

Abstract

Thin synchrotron-emitting filaments are increasingly seen in the intracluster medium (ICM). We present the first example of a direct interaction between a magnetic filament, a radio jet, and a dense ICM clump in the poor cluster A194. This enables the first exploration of the dynamics and possible histories of magnetic fields and cosmic rays in such filaments. Our observations are from the MeerKAT Galaxy Cluster Legacy Survey and the LOFAR Two-Meter Sky Survey. Prominent 220 kpc long filaments extend east of radio galaxy 3C40B, with very faint extensions to 300 kpc, and show signs of interaction with its northern jet. They curve around a bend in the jet and intersect the jet in Faraday depth space. The X-ray surface brightness drops across the filaments; this suggests that the relativistic particles and fields contribute significantly to the pressure balance and evacuate the thermal plasma in a ∼35 kpc cylinder. We explore whether the relativistic electrons could have streamed along the filaments from 3C40B, and present a plausible alternative whereby magnetized filaments are (a) generated by shear motions in the large-scale, post-merger ICM flow, (b) stretched by interactions with the jet and flows in the ICM, amplifying the embedded magnetic fields, and (c) perfused by re-energized relativistic electrons through betatron-type acceleration or diffusion of turbulently accelerated ICM cosmic-ray electrons. We use the Faraday depth measurements to reconstruct some of the 3D structures of the filameGnts and of 3C40A and B.

Unified Astronomy Thesaurus concepts: Radio jets (1347); Intracluster medium (858); Extragalactic magnetic fields (507); Extragalactic radio sources (508); Plasma physics (2089); Poor galaxy clusters (2006); Galaxy clusters (584)

Supporting material: animations

1. Introduction

The intracluster medium (ICM) is dynamic, driven by ongoing accretion along large-scale structure filaments and mergers with groups and clusters. There are additional internal injections of energy from supernova explosions as the embedded galaxies evolve, and less frequent but powerful injections of momentum, energy, cosmic rays, and magnetic fields from the jets of active galactic nuclei (AGN; Fabian 2012). Signatures of the dynamic ICM are visible in its X-ray emission in the form of shocks, cold fronts, large-scale ripples (Markevitch & Vikhlinin 2007; Sanders & Fabian 2007; Zhang et al. 2019), and surface brightness and/or temperature fluctuations (Churazov et al. 2012; Zhuravleva et al. 2014, 2016; Hu et al. 2022).

1.1. ICM Radio Features—the Emergence of Filaments

Radio emission provides a complementary window on ICM dynamics, including the distortions of tailed radio galaxy outflows, peripheral radio relics and cluster-wide halos primarily in merging clusters and their smaller mini-halo counterparts, typically associated with brightest cluster galaxies (BCGs) in more relaxed clusters (see, e.g., reviews by van Weeren et al. 2019; Rudnick 2019). These diffuse radio structures reveal the existence of a magnetized relativistic plasma, also seen through the Faraday rotation due to magnetic fields in the X-ray emitting thermal plasma (e.g., Bonafede et al. 2010). The diffuse radio structures typically require large-scale continuing inputs of energy to compensate for the radiative losses of the cosmic-ray electrons (Brunetti & Jones 2014).

Into this mix, a new radio phenomenon—filamentary structure—is emerging, as radio telescopes produce higher-resolution and sensitivity images (Knowles et al. 2022; Brienza et al. 2022). Their synchrotron emission and its accompanying polarization when there is sufficient sensitivity indicate that these are ordered magnetized structures (Govoni et al. 2005). Filaments themselves are not new; they have been known for a number of years to be prominent in radio galaxy lobes (Hines et al. 1989) and in the dramatic shock-related peripheral radio relic in A2256 (Owen et al. 2014; Rajpurohit et al. 2022b). However, isolated filaments are now also being observed in the ICM, not clearly associated with X-ray structures (e.g., Botteon et al. 2020). In addition, deep, high-resolution images of radio galaxies are revealing filaments in their surroundings; it is not clear if these are physically connected with the radio galaxies themselves or what they tell us about the underlying ICM magnetic fields (Ramatsoku et al. 2020; A1314 in van Weeren

et al. 2021; and Condon et al. 2021). There are several known cases where ICM magnetic fields are interacting with radio galaxies; these include the Faraday rotation banding seen across diffuse lobes (Guidetti et al. 2011, 2012) and the ram-pressure induced magnetic draping around fast-moving radio and nonradio galaxies (Müller et al. 2021, 2021).

Filamentary structures present new opportunities for studying the physical processes in the ICM, including their magnetic structures and the evolution of cosmic rays. In merger-driven flows, they can serve as probes of shear motions, which are otherwise invisible, and reveal the driving and dissipation scales of dynamic structures as the cluster evolves. Their widths can provide information about the resistivity scales in the plasma. Filamentary structures may also arise when these flows interact with bubbles of old emission from AGN (ZuHone et al. 2021), although the appearance of the filaments is heavily dependent on the modeling of the cosmic-ray physics (ZuHone et al. 2021). In this paper, we investigate a prominent pair of filamentary structures in A194 that shows clear signs of interactions with the northern jet from 3C40B, associated with the BCG NGC 547.

Isolated filaments may provide yet another site for cosmic-ray acceleration in clusters. Cosmic-ray electron reacceleration to energies of several GeV is already required for diffuse radio structures such as relics and halos to be visible at GHz frequencies. For halos, turbulent reacceleration throughout the cluster appears to be the most promising, while peripheral radio relics are likely associated with (re-)acceleration at shocks produced from mergers (see the review by Brunetti & Jones 2014). Bell et al. (2019) examined reacceleration in magnetic flux tubes in the backflows of radio galaxies, which would appear as filamentary features; they concluded that repeated encounters with weak shocks in such tubes could accelerate electrons to extremely high energies. While the backflow tubes likely differ from the filamentary structures found in the external ICM, they illustrate the possibility that mechanisms associated with tubes might play an important role.

Ultimately, the seed electrons upon which the reacceleration operates likely come from current or past AGN activity. Whether we can link specific filamentary structures to individual radio galaxies (as in cases where bars directly cross a tailed radio galaxy; Venturi et al. 2022; Lame'e 2017; Botteon et al. 2020) or where they appear to be the remnants of a dissipating lobe (Brienza et al. 2022), or whether multiple AGN contribute to a mixed-background seed population, or whether both play a role, are major open issues.

Filamentary structures are a natural consequence of turbulence in a high-β (high ratio of plasma to magnetic pressure) magnetized plasma. Simulations show that extended bundles of magnetic fields, which would be observed as filaments, are ubiquitous in turbulent magnetohydrodynamics (MHD) flows where their lengths reflect the local driving scales of the turbulence (Porter et al. 2015). These filamentary structures are formed from the tearing of thin current sheets; they are then stretched until the magnetic stresses approach the dynamical turbulent stresses. Driven by ongoing merger activity, e.g., these filaments can reach cluster scales (Vazza et al. 2018).

Except in the presence of shocks, the sound speeds in the ICM ($\sim 10^3$ km s^{-1}) enforce pressure equilibrium. When the dynamic pressure of AGN jets allows them to propagate in the ICM, the conversion of this directed energy into thermal energy can then evacuate cavities in the X-ray emitting plasma

(Churazov et al. 2000; McNamara et al. 2000). One such cavity was previously reported in A194, associated with the southern lobe (Bogdan et al. 2011). However, if the magnetic pressures in filamentary structures, along with the accompanying cosmic-ray pressure, can approach those in the surrounding medium, then they also may be sufficient to exclude the thermal plasma. Thus, cavities in the X-ray ICM may appear even when there is no conversion from dynamic into thermal pressure. This new physical process in the ICM is explored further below.

1.2. A194

A194 is a richness class 0 BMII galaxy cluster (Abell et al. 1989) at a redshift of 0.018 (Struble & Rood 1999).[8] As reported by Lovisari et al. (2015) from XMM-Newton observations, A194 exhibits a low X-ray luminosity ($7.1 \pm 0.7 \times 10^{42}$ erg s^{-1}, 0.1–2.4 keV) and a low X-ray temperature ($kT = 1.37 \pm 0.04$ keV), which is characteristic of an X-ray bright group. The region of a superposed contaminating cluster at redshift 0.15 was removed from the analysis by Lovisari et al. (2015) to derive the global parameters of A194. The hydrostatic mass yields $M_{500} = 2.8 \times 10^{13}$ $M_\odot$, which corresponds to $R_{500} = 460$ kpc ($21'$) at the distance of A194. Applying the scaling factor of 1.5 by Šuhada et al. (2011), this yields $M_{200} = 4.2 \times 10^{13}$ $M_\odot$ based on the hydrostatic X-ray derived cluster mass.

Optically, Govoni et al. (2017) analyzed the spatial distribution and spectra for 143 cluster member galaxies. They found a 1D velocity dispersion of $\sigma = 425^{+34}_{-30}$ km s^{-1} and two primary subgroups, both elongated in the NE–SW orientation (see Figure 4 of Govoni et al. 2017). They conclude that there is no strong evidence of a major merger, but ongoing accretion of small groups along the NE–SW axis. Rines et al. (2013) performed a caustic analysis of A194. The derived velocity dispersion within R_{200}, $\sigma = 402^{+38}_{-29}$ km s^{-1}, is consistent with the analysis of Govoni et al. (2017). The associated mass is $M_{200} = 1.1 \times 10^{14}$ $M_\odot$ which is significantly higher than the X-ray value of Lovisari et al. However, Govoni et al. (2017) could only trace the X-ray temperature profile to $\sim 0.6 R_{500}$, so this higher derived cluster mass is based on extrapolation.

1.2.1. Previous Radio Observations of A194

A194 has been the subject of multiple radio studies (O'Dea & Owen 1985; Jetha et al. 2006; Sakelliou et al. 2008; Bogdan et al. 2011; Govoni et al. 2017). Most focused on the emission from the two prominent radio galaxies 3C40A and 3C40B. 3C40A contains the well-studied Minkowski's object, a region of intense star formation that has likely been triggered by the impinging jet (Brodie et al. 1985; van Breugel et al. 1985; Croft et al. 2006). The prominent eastern filaments in A194 (hereinafter *E-fils*), which are the focus of the current paper, were observed and described as the double-stranded trail by Sakelliou et al. (2008), who also were able to measure the steepening of the spectrum as they extended eastward from their intersection point with the northern jet of 3C40B. Govoni et al. (2017) measured polarization structures in the A194 system, combining archival 1.5 GHz VLA data with low-resolution single-dish 6.6 GHz data from the Sardinia Radio Telescope. At low resolution, the *E-fils* are seen as a high-polarization stub. At higher resolution, Govoni et al. (2017)
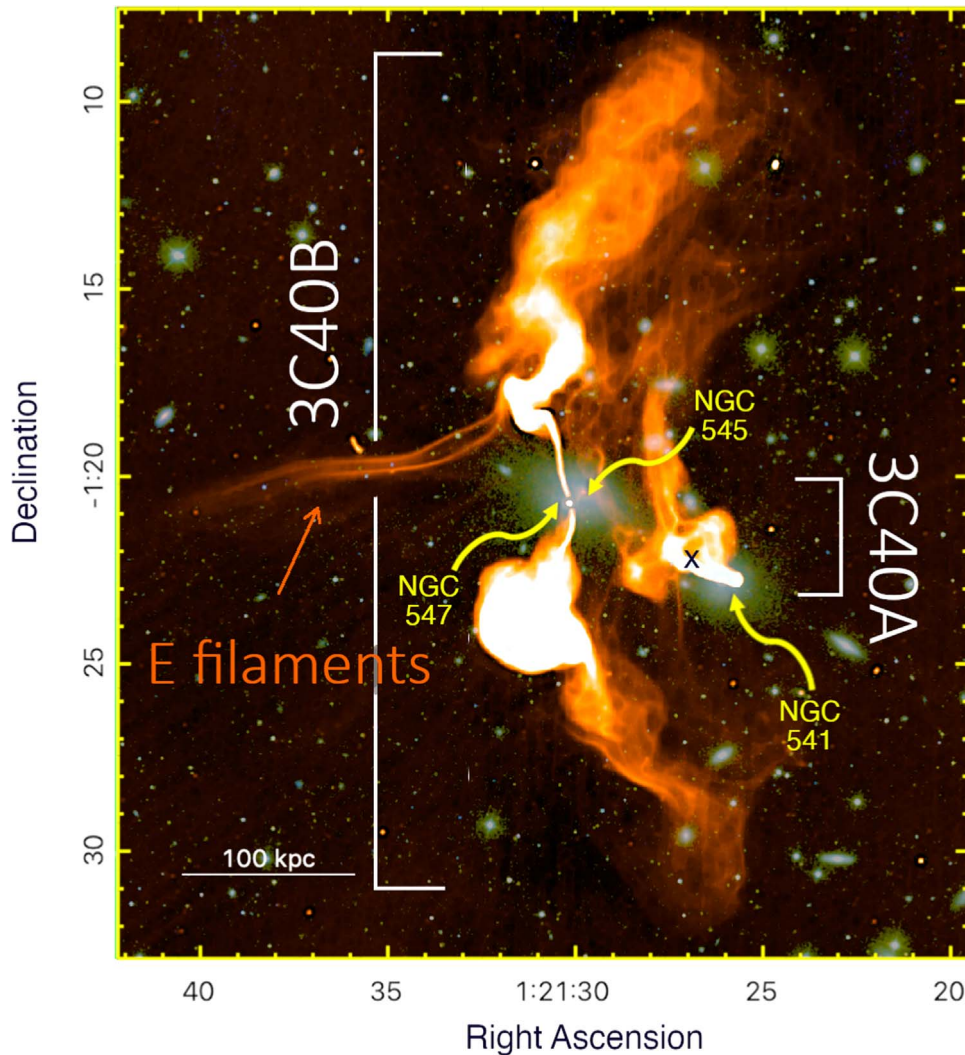
Figure 1. Radio frequency map at 7″.75, identifying the main features under discussion. A small amount of edge enhancement has been added to emphasize the fine-scale features; this image is not to be used quantitatively. Overlaid on optical SDSS *gri* images (Alam et al. 2015). The X marks the location of Minkowski's object.

measured low values of the rotation measure (RM), and very high fractional polarization of the *E-fils* (1.0 ± 0.25) with a magnetic field aligned along the filaments, all features that are confirmed and shown in more detail here. Most recently, the MeerKAT Galaxy Cluster Legacy Survey (MGCLS; Knowles et al. 2022) presented high-resolution total intensity and spectral images of A194, revealing the dense network of filamentary structures and the prominent *E-fils* ; these same data form the basis of the more detailed investigations in this paper.

The region under study in this paper extends out to only ∼330 kpc from the cluster center. For context, this is somewhat larger than $R_{2500} = 197 \pm 11$ kpc (Lovisari et al. 2015), while the caustic radius of A 194 extends beyond ∼8 Mpc (Rines et al. 2013).

1.3. Paper Plan

Figure 1 introduces the objects under discussion in the paper, primarily the *E-fils* and the large (>500 kpc) radio galaxy 3C40B. In Section 2 we describe the observations, and Section 3 presents a global view of the cluster data products. A more detailed look at the *E-fils* and the region where they intersect the northern jet is given in Section 4. The underlying physical issues of the jet/filament interaction are explored in

Section 5, with concluding remarks and recommendations for further studies in Section 6.

2. Observations and Initial Map Production

2.1. MeerKAT

MeerKAT[9] observations were conducted in full polarization mode in the *L* band, 900–1670 MHz, as described in Knowles et al. (2022). Telescope parameters are described in detail in Jonas & MeerKAT Team (2016) and Camilo et al. (2018). The primary beam size at the band center of 1.28 GHz was 1.2°; all of the observations presented here lie in the central 0°.5. The rms noise was 5.7 μJy beam^{-1} near the field center, with a nominal beam size of 7″.69×7″.55 at position angle 88°. After self-calibration, final images were produced and cleaned using the OBIT[10] (Cotton 2008) wide-band wide-field imager MFImage, using robust weighting (−1.5), facets to correct for sky curvature, and a frequency-dependent taper to maintain an approximately constant resolution over the ∼2:1 frequency range (see Cotton et al. 2018). The images were in the form of

---

[9] Operated by the South African Radio Astronomy Observatory (SARAO).
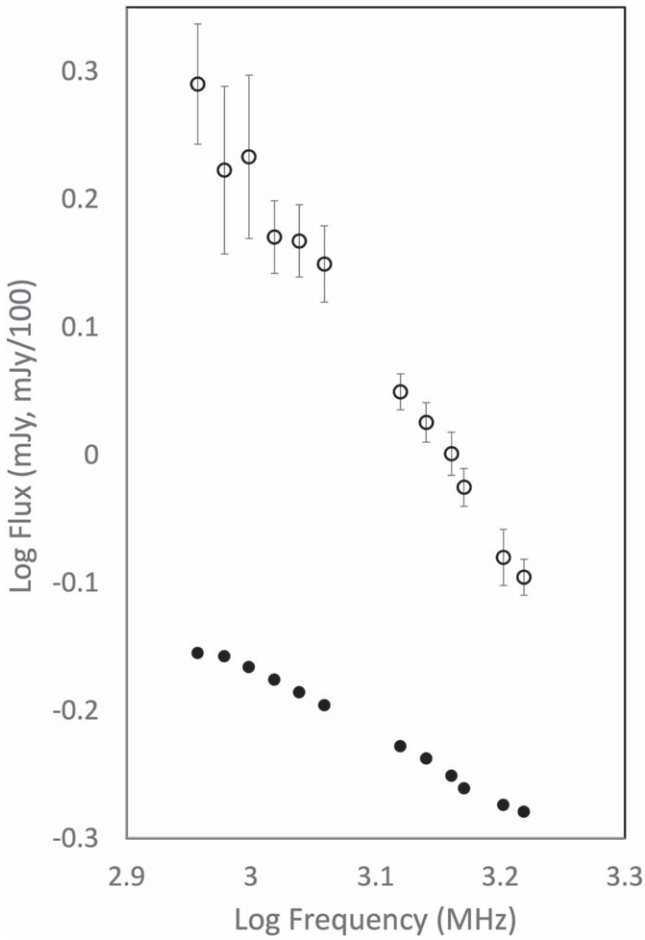[10] http://www.cv.nrao.edu/bcotton/Obit.html

Figure 2. Plots of log(Intensity) vs. log(Frequency) for two illustrative positions to show the quality of the spectral information. These are from maps convolved to 15″ and represent the averages over small boxes on the filament (open circles) and at the first turn in the northern jet (point A in Figure 20, filled circles) after dividing the fluxes by 100 for display purposes. Statistical errors for the jet are smaller than the symbol size, although the nonlinearities are probably due to residual bandpass calibration errors.

14 frequency channel cubes, each with a 5% fractional ($\Delta\nu/\nu$) bandpass. The quality of the data for calculating spectra are illustrated in Figure 2, showing one faint and one bright region. The spectral indices were calculated from a nonlinear least-squares fit to $I(\nu) = I_0 \nu^\alpha$ for the 14 channels.

Polarization calibration and mapping was done as described in Condon et al. (2021) and Knowles et al. (2022), using a series of steps to fix the polarization angle and rotation measure of 3C286 to $-33°$ and zero, respectively (Perley & Butler 2013). To better track the Faraday induced variations in Q and U, we divided the band into 68 frequency channels. Examples of the initial polarization results (polarized intensity, rotation measure, and zero wavelength polarization angle) were derived from RM Synthesis (RMFit:Cube), using the peak value in the Faraday spectrum at each pixel. Unless noted otherwise, no normalization was done for the total intensity spectrum at each pixel; this does not affect the peak RM, as presented, but would broaden the observed Faraday spectrum. Results are also presented from a new procedure (RMSyn) which achieves higher resolution in Faraday space by a factor of ~3 (W. Cotton & L. Rudnick 2022, in preparation). The width of the restoring beam for the clean components is fixed
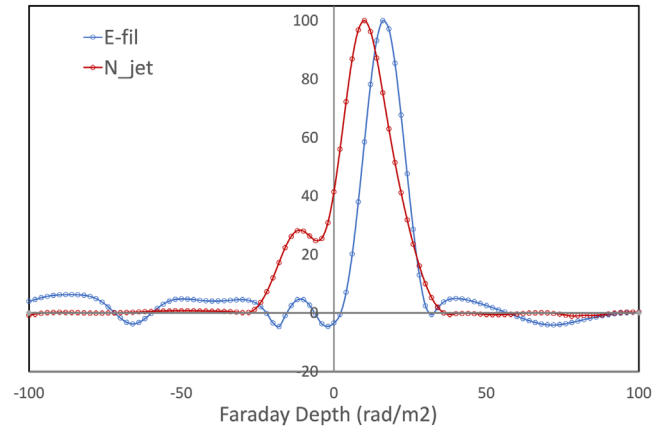

Figure 3. Faraday spectra, normalized to the same peak brightness, from the high resolution Faraday-cleaned spectrum for two illustrative locations, one on the southern filament of the *E-fils* structure ($01^h26^m13^s76$, $-01^d13^m37^s$, blue) and one at the location of an unresolved X-ray feature (see below) near the intersection of the northern jet with *E-fils* ($01^h26^m06^s12$, $-01^d19^m37^s$, red). The filament is only marginally resolved spatially, with an observed width in Faraday space of 13.6 rad m^{-2}, while at the X-ray feature, there is Faraday structure over scales of >20 rad m^{-2}.

by the real part of the dirty beam created using $\lambda_0^2 = 0$ instead of the standard $\lambda_0^2 = \langle\lambda^2\rangle$ averaged over the range of observations (Brentjens & de Bruyn 2005). Figure 3 shows the Faraday spectra for two illustrative locations, restored with a Faraday beamwidth of 15.6 rad m^{-2}; these are used to determine the peak rotation measure and the polarized intensity. We used these measurements to characterize the fractional polarization, rotation measure, and polarization position angle along the filaments by sampling them at the same locations as the total intensity.

2.2. LOFAR

3C 40B was observed with LOFAR (van Haarlem et al. 2013) as part of the LOFAR Two-meter Sky Survey (LoTSS; Shimwell et al. 2017, 2019, 2022) in pointing P020 + 01. Observations for this pointing were taken on January 7 and 2019 May 16, each observation having an integration time of 4 hr and covering the 120–168 MHz range. The data reduction was performed in a standard way following the prefactor and Data Release 2 DDF-pipelines (Tasse et al. 2021). These pipelines include flagging (Offringa et al. 2012), calibration for direction-independent (Williams et al. 2016; de Gasperin et al. 2019) and direction-dependent effects (Tasse 2014), and applying the calibration solutions during imaging (Tasse et al. 2018). The target visibilities were subsequently extracted by subtracting all sources in the field of view from the visibilities, except for the 0.75 square degree region around 3C 40B. The calibration for 3C 40B was further optimized by carrying out a self-calibration procedure as described in van Weeren et al. (2021), using the WSClean imager (Offringa et al. 2014) with multiscale deconvolution (Offringa & Smirnov 2017). The final LOFAR image is made with Briggs robust -0.5 weighting, (equivalent to ≈ -1.5 in the AIPS/ OBIT implementations) and has an rms noise of 0.42 mJy beam^{-1}, with a beam size $14''.7 \times 6''.5$.

There is a large uncertainty in the LOFAR flux scales. We thus used 11 compact sources in the field and measured their spectral indices $\alpha(144, 1283)$ between the LOFAR and MeerKAT maps at 15″ resolution, and the $\alpha(900 - 1670)$

indices determined from fitting across the 15″ MeerKAT frequency maps. The compact sources were observed to scatter around the power-law line, as expected for their spectra, with a correction of −0.085 to the low-frequency spectral indices. This represents a gain correction of ∼1.2 to the nominal LOFAR map values. This correction was adopted for all further measurements. There were several other compact sources in the field with spectra flatter than −0.5; these were not used in the analysis because neither their likely true spectral shapes nor the effects of possible variability are known.

2.3. X-Rays

We employed archival X-ray data of A194 from ESA's X-ray Multi-Mirror Mission (XMM-Newton; Obsid 0743700201, PI Farrell), taken in January 2015. This observation consisted of five exposures with the European Photon Imaging Camera (EPIC), one 130ks PN observation, and two MOS1 and two MOS2 observations with 87/50ks each. We processed the data with the XMM-Newton SAS software package version 19.0.0 and used the XMM-Newton-Extended Source Analysis Software (Snowden et al. 2008) to produce exposure-corrected and background-subtracted images. The light-curve cleaning was performed with the mos-filter and pn-filter tools, resulting in a usable exposure time free of solar flares of 65ks for PN and 171ks for MOS. We followed the standard procedure described in the ESAS Cookbook[11] and produced combined images in the 0.4–1.25 keV band, as well as in the 1.25–3 keV band.

3. The Global View

We start by summarizing the key observational findings. Readers with a primary interest in the physical interpretations may find it useful to skip to Section 5 and refer back here as needed.

1. The *E-fils* have narrow emission extending ≳200 kpc and more diffuse emission extending ∼300 kpc from the 3C40B jet, with narrow components ∼3–8 kpc across and a broad component relatively constant at 12 kpc wide (FWHM).
2. Minimum pressures in the *E-fils* are ∼1–2 × 10^{-12} (10^{-11}) erg cm^{-3}, assuming proton/electron ratios of 1 (100). The local X-ray pressures are ∼10^{-11} erg cm^{-3}.
3. The magnitude of the line-of-sight component of the ICM magnetic field, calculated using the Faraday structure, is estimated to be 1.4 μG near the bends in the northern jet, at a distance of ∼75 kpc from NGC 547; the minimum pressure field in the jets themselves is four times higher.
4. There is a ∼20% deficit in X-ray surface brightness at the position of the *E-fils*, consistent with an absence of X-ray emitting material in a ∼35 kpc cylinder encompassing the radio structure.
5. The spectra of the *E-fils* steepen mostly monotonically with distance from 3C40B, from about −1.3 to −2.5, likely reflecting the increasing dominance of the steep-spectrum diffuse emission relative to the flatter spectrum narrow components. The spectra show convex curvature, significantly smoother than exponentially cutoff spectra. The spectral shape of the *E-fils* in the curved region is

indistiguishable from the spectral shape of the emission from 3C40B.
6. The *E-fils* are ∼50% polarized, with no detectable net RM with respect to the Galactic foreground, and only small rms variations (9 rad m^{-2}) along their length. This enables a mapping between Faraday depth[12] and distance along the line of sight, revealing their 3D structure.
7. The *E-fils* are bent and wrap around the northern jet of 3C40B as it abruptly turns to the west and expands. The Faraday depths of the jet and *E-fils* also coincide at this point, indicating that this is a physical interaction in 3D, rather than a chance superposition along the line of sight.
8. There is an isolated unresolved X-ray feature of indeterminate origin at a sharp bend in the 3C40B jet, where it intersects with the *E-fils*.

A global view of the data products used in this paper is given in Figure 4. The total intensity radio image from MeerKAT (first presented in Knowles et al. 2022) identifies the two central radio galaxies in A194, 3C40B—the subject of this paper—and 3C40A. These radio sources are embedded in a rich network of filaments. Some of these, such as those extending north from 3C40A, appear to be extensions of the radio galaxy; others, especially between 3C40A and 3C40B, are not clearly connected to either source. The most prominent filaments are the *E-fils*, seen to extend over 200 kpc east of 3C40B; they are studied in detail below. An additional view of the filamentary structures, including those found inside the lobes of 3C40B, is presented in Appendix A.

The brighter central regions of the X-ray emission from XMM-Newton are also seen in Figure 4, overlaid with the MeerKAT image. The bright patch at the southwest end of the diffuse X-ray emission is from a background cluster at $z = 0.15$ (Mahdavi et al. 2005). A pointed ROSAT PSPC image (Bogdan et al. 2011) shows that the X-ray emission extends for ∼37.′5 (∼800 kpc) along a NE–SW axis, far beyond that visible in this image. Bogdan et al. (2011) also detected an X-ray cavity associated with the southern lobe of 3C40B.

Figure 4 also shows the in-band spectral indices of the radio galaxies. The bright regions of 3C40B north have a spectral index of ∼-0.5 and show no characteristic steepening with increasing distance from the core until there is a significant drop in brightness at a distance of ∼100 kpc. In the south, the -0.5 spectral regions extend for a similar distance from the core, although they are embedded in slightly steeper emission in the southern lobe. The spectra continue to steepen farther out, although the signal-to-noise ratio (S/N) at the 7.75″ resolution shown here is too low to produce reliable indices for the fainter filamentary structures. A more detailed discussion of spectral trends in the *E-fils* is presented below.

The final data product previewed in Figure 4 illustrates the rich Faraday structure available for this system. Unlike other images in the literature, this is not a Faraday RM image, although it is closely related. Instead, Faraday synthesis often reveals a distribution of Faraday depths, as opposed to a single RM, along individual lines of sight.[13] The colors here result from various combinations of emission at different Faraday

---

[11] https://heasarc.gsfc.nasa.gov/docs/xmm/esas/cookbook/xmm-esas.html

[12] A Faraday spectrum represents the brightness of the polarized emission at a given location as a function of Faraday depth (Brentjens & de Bruyn 2005). In the simplest case, where emission is observed at only one Faraday depth, this depth is equivalent to the more commonly used term "rotation measure" (RM).

[13] Where the Faraday spectrum is dominated by a component at a single Faraday depth, this depth is designated the RM.
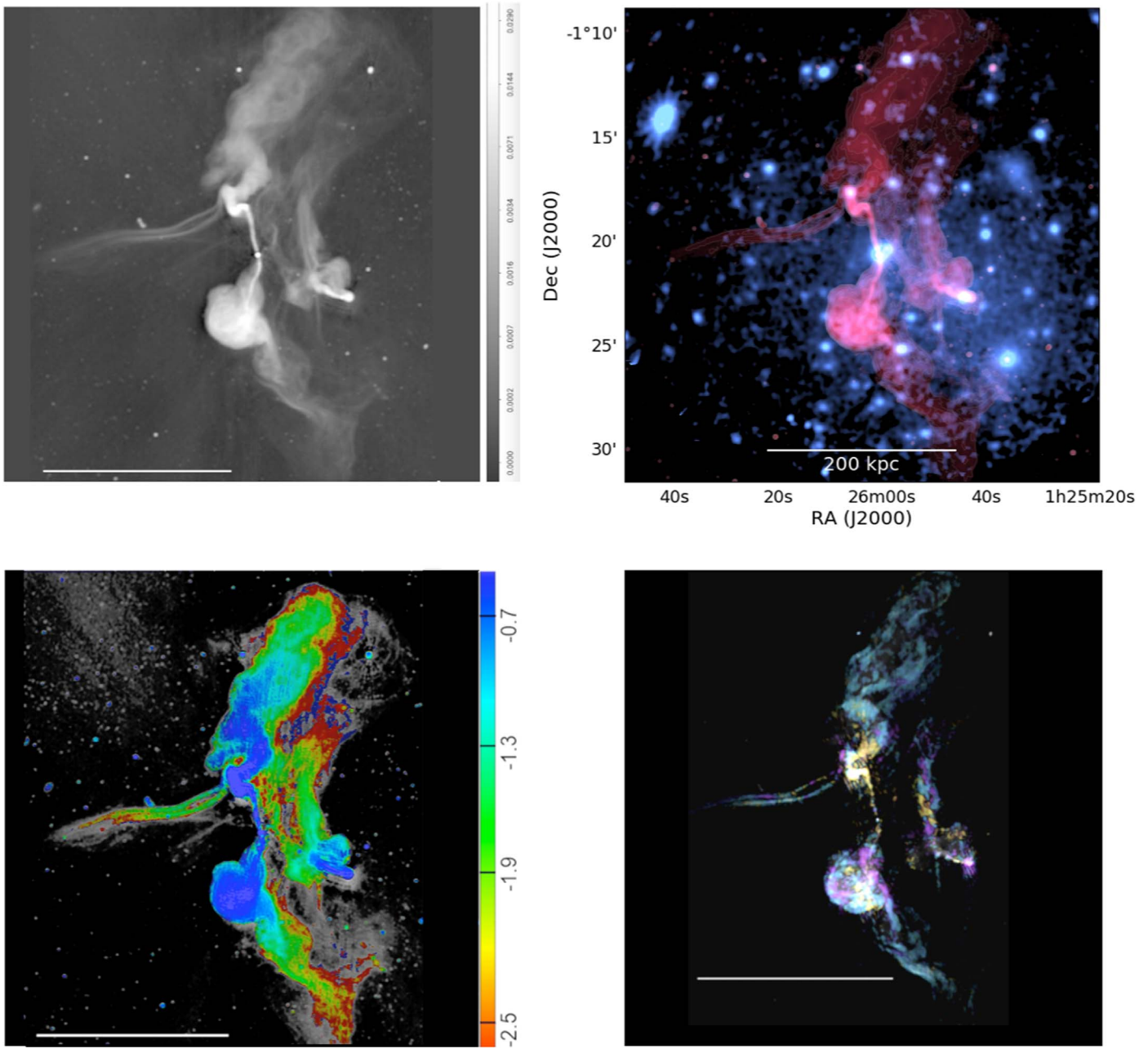
Figure 4. All radio images are at $7\rlap{.}{''}75$ resolution. Top left: total MeerKAT intensity image, showing the intensity scale. Top right: overlay of MeerKAT total intensity image in pink with the XMM-Newton image in blue. Bottom left: spectral index image with regions in gray indicating the low S/N regions at this resolution, where no good spectral fits were achieved. Bottom right: Faraday depth composite, to illustrate the rich Faraday structure, color-coding the emission at a range of Faraday depths from -14 to 50 rad m^{-2}. Since emission from multiple Faraday depths contributes to each pixel, there is no simple translation from a single color into a single Faraday depth. Yellowish (blue, purple) colors tend to be dominated by emission at approximate depths of -10 (10, 40) rad m^{-2}. The images each have a bar indicating a length of 200 kpc ($552''$).

depths and simply illustrate the complex structures. Figure 5 shows the distribution of the peak RMs (which have a spread of $\sim$9 rad m^{-2}), and the fuller picture of the Faraday depth distribution (with a spread of $\sim$34 rad m^{-2}) from summing the power in the image at each depth.

3.1. The Diffuse Emission

In order to probe the lowest-brightness emission in A194, we filtered the LOFAR image using the multiresolution filtering technique of Rudnick (2002), with a box size of $76\rlap{.}{''}5$, and then convolved it with a $75''$ beam. The results are shown in

Figure 6. Note that this diffuse emission represents only emission on scales $\gtrsim 75''$; it is not a low-resolution version of the total intensity image, in which the convolved finer-scale emission would completely dominate the brightness. The diffuse component of the *E-fils* is seen to extend to $\sim$850$''$ (300 kpc) from 3C40B's jet. Near the end, its brightness is $\sim$6.7 μJy/$('')^2$. The bright portions of the radio galaxies 3C40A and B and their surrounding filamentary structures are all embedded in a low-brightness region of $\sim$60 μJy/$('')^2$. Faint emission covering a region $\sim$200 kpc across can also be seen south of the *E-fils*, at a level of $\sim$1.6 μJy/$('')^2$, without an obvious association with other radio structures.
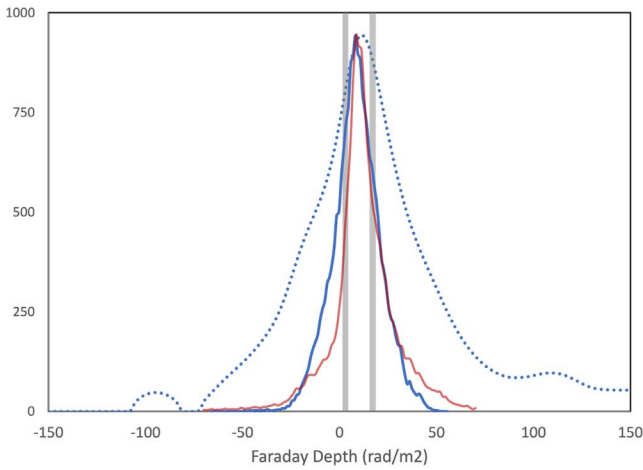
Figure 5. Distribution of Faraday depths in the central regions of A194, encompassing 3C40B, 3C40A, and the surrounding filamentary features. The red line shows peak RMs from the standard Faraday synthesis. The blue line shows the first moment in Faraday depth space of the amplitude of the high resolution Faraday spectrum in each spatial pixel. Both of these used only polarized intensities $\gtrsim 150\ \mu$Jy beam^{-1}. The dashed blue line is the sum of the power in each Faraday depth channel, with a noise contribution subtracted in quadrature. This includes all the polarized emission, on and off the peak in the spectrum. The approximate range of Faraday depths produced by the foreground Milky Way is shown in gray.
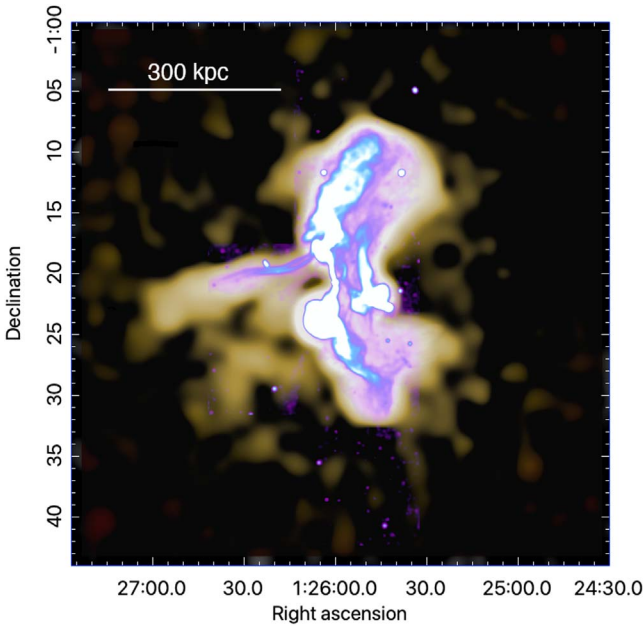

Figure 6. Overlay of 15″ MeerKAT image (purple) onto diffuse LOFAR emission (yellow) at 75″ resolution, as described in the text, showing the 300 kpc extent of the diffuse component of the *E-fils*.

4. The East Filaments

4.1. Structure

The *E-fils* consist of a pair of narrow, curved, mostly parallel structures embedded in a more diffuse background that traces a similar locus. The total extent of the filaments is ~600″ (220 kpc) along their curved path, with a very diffuse extension to 300 kpc shown above. Their total flux at 1283 MHz is ~80 mJy, corresponding to a monochromatic luminosity of 10^{19} W/Hz. Additional low surface brightness regions and
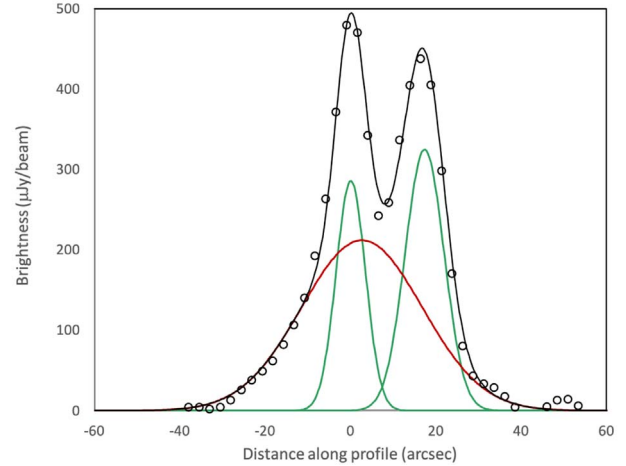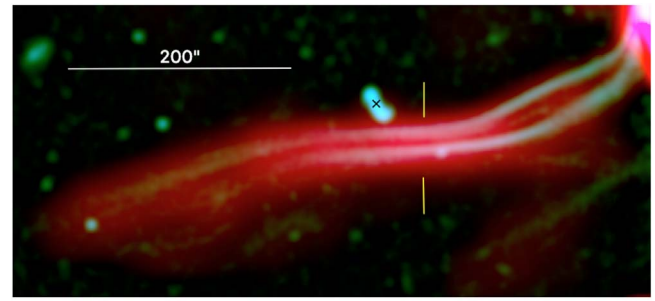

Figure 7. Top: the eastern filaments separated by color into narrow and broad components, as described in the text. The black X marks the location of an unrelated background radio double, at R.A. 01:26:23.41, decl. -1:19:10. Bottom: profile across the eastern filaments as indicated by the broken vertical yellow line. The data are shown as open circles with errors on the same order as the symbol size. The solid curves show a three-Gaussian fit, with two green narrow components, one red broad component, and the total fit shown in black.

faint intersecting filaments at different angles are also present in this region; these are fainter than seen in the maps presented here and are not obviously connected to the *E-fils*. The brightnesses, and thus emissivities of the *E-fils*, are a factor of 10^{4} below those of the 3C40B jets.

The *E-fils* are at least slightly resolved in most places in our 7.75″ maps and are a combination of narrow and broad features, which can be seen in Figure 7. For this figure, the separation between narrow and broad features was done using the multiresolution filtering method of Rudnick (2002) using a box size of 30″. The broader features are enhanced in the color figure to increase their visibility. To illustrate the actual typical relative brightness contributions of these components, Figure 7 shows a north–south profile cut near the midpoint of the filament structure, along with a three-Gaussian fit. The deconvolved narrow component widths are 0.85 ± 0.2 kpc (south) and 2.8 ± 0.1 kpc (north), while the broad component width is 12 ± 0.2 kpc. Across this strip, the brightnesses of the narrow and broad components are comparable, as well as their total fluxes of 750 μJy and 910 μJy, respectively, from integrating along the 7.″75 strip. The relative contributions of narrow and broad features changes along the filaments; closer to 3C40B, the narrow components dominate, while the broad component dominates farther to the east (Figure 8). Trends of brightness and other parameters along the *E-fils* are presented below.
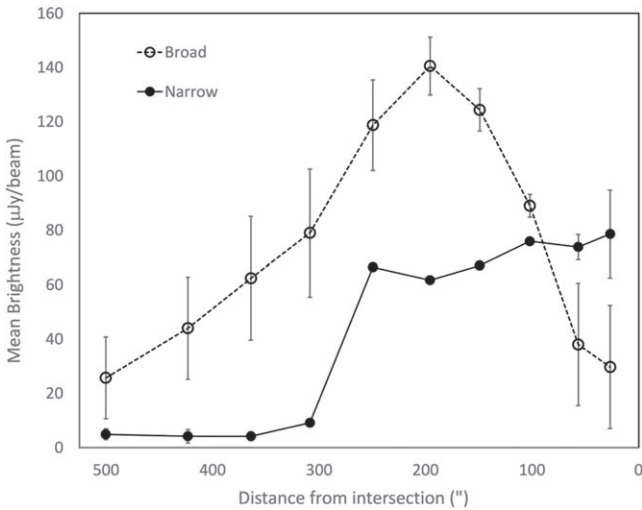
Figure 8. Average brightness in boxes of the broad and narrow emission as a function of position along *E-fils*. The 7.″75 maps were decomposed into broad and narrow components using the multiresolution filtering technique of Rudnick (2002) with a (somewhat arbitrary) box size of 30″ (11 kpc). The details, but not the overall trend, would change with a different choice of box size.

4.2. Spectra

To characterize the intensity and the spectral and polarization behavior along the *E-fils*, we calculated the mean of the respective quantities in small boxes (1–2 beam areas) positioned along the ridge line of the N and S *E-fils* in the 7.″75 maps.

The peak brightnesses of the *E-fils* occur in a broad region ∼200″ from where they intersect with 3C40B (Figure 9) while the spectra steepen mostly monotonically with distance from 3C40B. The steepening spectra could result from four different causes: (a) A decrease in particle energies due to radiative and/ or adiabatic losses as a function of distance from 3C40B (e.g., if the electrons were streaming from 3C40B). (b) A decrease in the magnetic field strength away from 3C40B, so that for a fixed electron energy distribution falling off at high energies (assuming no particle acceleration), higher-energy electrons (and thus steeper spectra) would be sampled at larger distances. (c) A decrease in the relative strength of the narrow and broad components of *E-fils*, as discussed below. Finally, (d) changes in the local relativistic particle acceleration processes as a function of distance away from 3C40B.

It would be very useful to separate the spectral indices as a function of position separately for the narrow and diffuse components of *E-fils*. However, at full resolution, there was insufficient S/N to measure the low-brightness emission, and at lower resolution, there is too much blending between the components. To increase the S/N at full resolution, we convolved the 15″ maps by 35″ along *E-fils* and made transverse profiles at each frequency. At one position, both the narrow and broad emission were strong enough to determine their spectra simultaneously, and the results are shown in Figure 10. The narrow filaments had spectra of -1.3 ± 0.07 (north), -1.8 ± 0.08 (south) and the broad component -2.7 ± 0.2. These values are very similar to those shown in Figure 9, where each of these components dominate the emission. It is plausible and even likely that the spectral steepening as a function of position along the jet is due to the
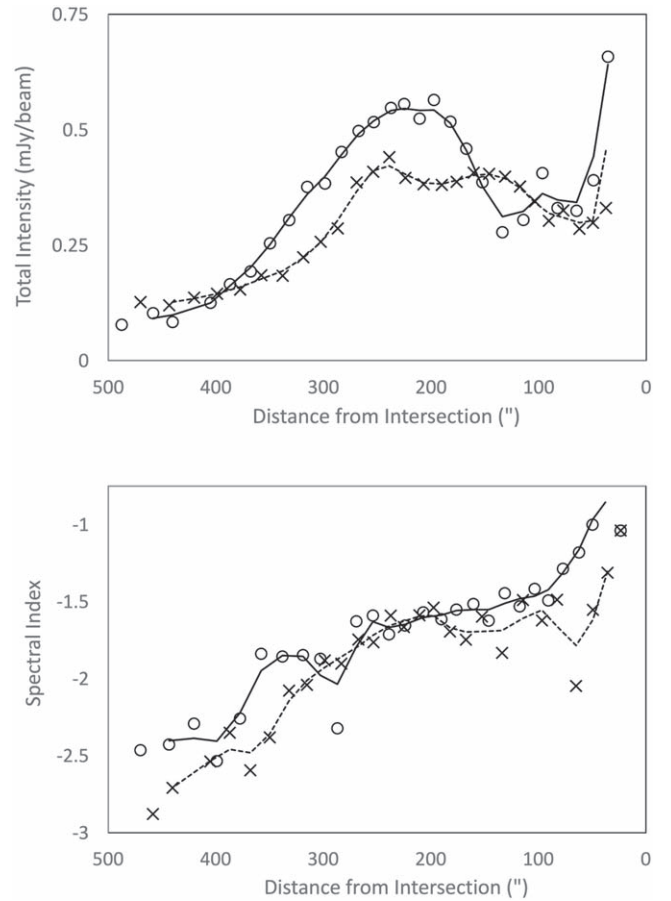

Figure 9. Intensity (top) and MGCLS in-band spectral index (bottom) as a function of distance from the intersection of *E-fils* with 3C40B, highlighting the nearly monotonic spectral steepening with distance. Values are from the means in small boxes along the ridge lines of the north (circles, solid line) and south filaments (Xs, dotted line). Lines are Hanning smoothed.

changing relative dominance of the diffuse and fine-scale emission, as shown in Figure 8

To characterize the shape of the relativistic electron population, we used measurements at 15″ resolution of the spectral indices between 960 MHz and 1670 MHz ($\alpha_{900-1670}$[14]) and between 1283 MHz (the central MGCLS frequency) and the LOFAR map at 144 MHz, convolved to 15″. ($\alpha_{144,1283}$). Both of these spectral index maps are shown in Figure 11 for the region containing the *E-fils* and the bright northern region of 3C40B.

We used the color–color diagram in Figure 12 (Katz-Stone et al. 1993), plotting $\alpha_{900-1670}$ versus $\alpha_{144,1283}$, to examine the shape of the underlying spectra, using the correction to the LOFAR flux scale described earlier. If the shape of the underlying population of electrons is the same throughout a source, then there is a unique mapping between the locus of points from different positions in the source and the shape of the spectrum in $\log(I)$ vs. $\log(\nu)$ space. Changes in local magnetic field strength shift the observed spectrum in $\log(I)$ vs. $\log(\nu)$ space, but preserve the locus in color–color space. The same is true for adiabatic changes to the electron energy distribution. The locus is unchanged even in the

---

[14] Values of $\alpha_{900-1670}$ at 15″ resolution are available as an MGCLS data product, derived from fitting the 15″ total intensity images as a function of frequency across the MeerKAT GCLS band, as described in Knowles et al. (2022).
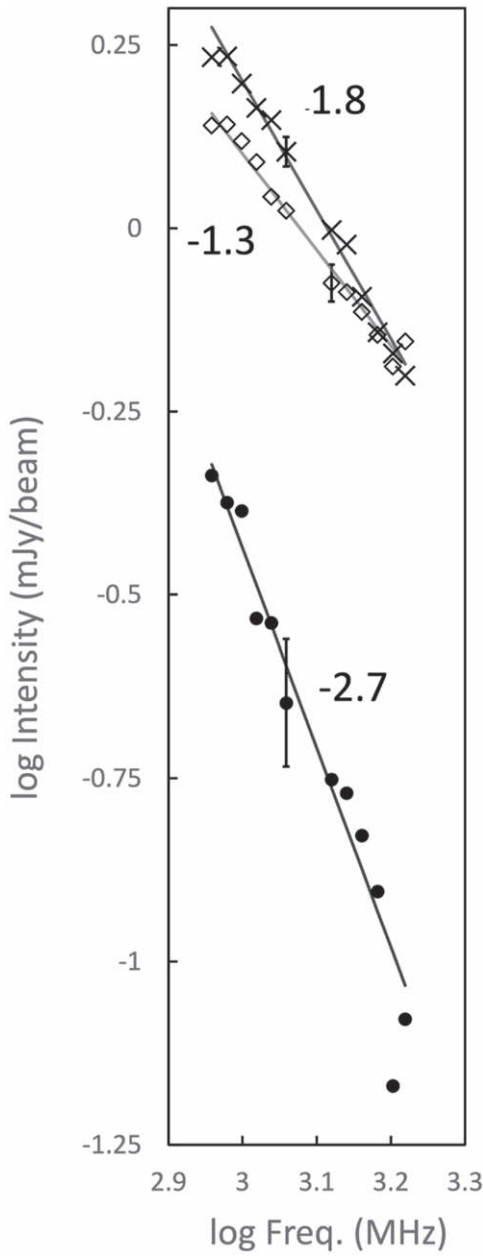
Figure 10. Spectra of the north (Xs), south (diamonds), and broad (filled circle) components from a transverse cut across *E-fils* after convolving each frequency channel by 35″ along the structure. Typical errors are shown.

Figure 11. Total intensity maps at 15″ resolution, color-coded by spectral index. Top: MeerKAT image with $\alpha_{900-1670}$. Bottom: LOFAR image with $\alpha_{144,1283}$. The color scales are the same, so the low-frequency indices are flatter, as expected for convex spectral shapes.

presence of radiative losses for idealized energy distributions (Katz-Stone et al. 1993). The locus of points occupied in the color–color diagram thus can be used to determine the shape of the underlying electron population. However, this can become difficult to interpret when each line of sight contains regions with different magnetic field strengths, or different particle gain/loss processes (e.g., Stroe et al. 2014).

The results of the color–color analysis are shown in Figure 12 for both 3C40B and the eastern filaments. For 3C40B, the spectra were averaged over boxes with sizes that increased at low brightness levels to increase the S/N. For the relatively faint filaments, we calculated the spectra over large areas (∼50 beams) in two different ways to check their robustness. Filled circles represent noise-weighted spectra
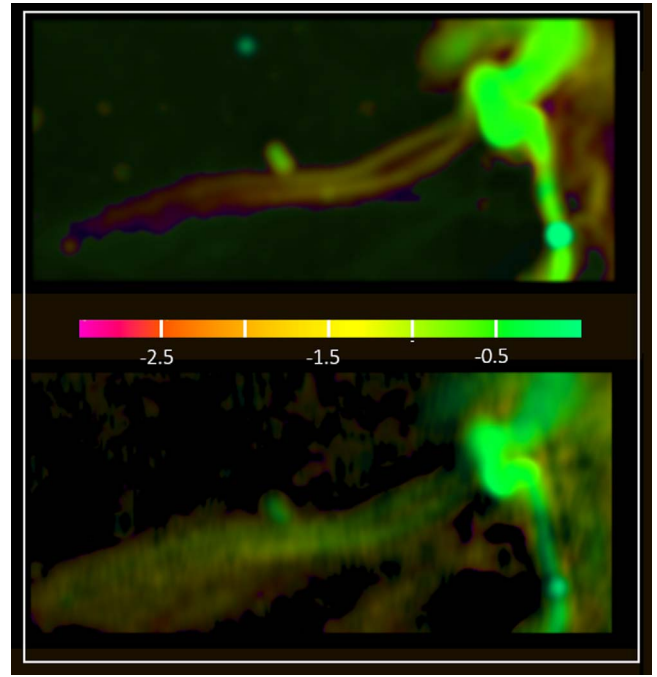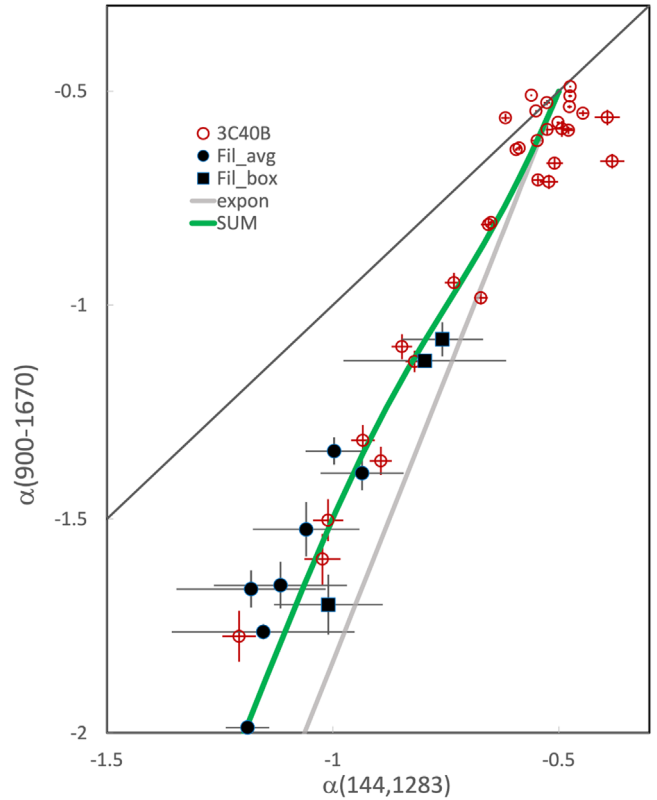

Figure 12. Color–color diagram for 3C40B (red) and *E-fils* (black symbols, see description in text). For comparison purposes, we show the line corresponding to power laws with different slopes (black), an exponentially cutoff spectrum with a low-frequency index of −0.5 (gray) and an illustrative sum of two cutoff spectra with different cutoff frequencies in solid green, as described in the text. See also Figure 13.
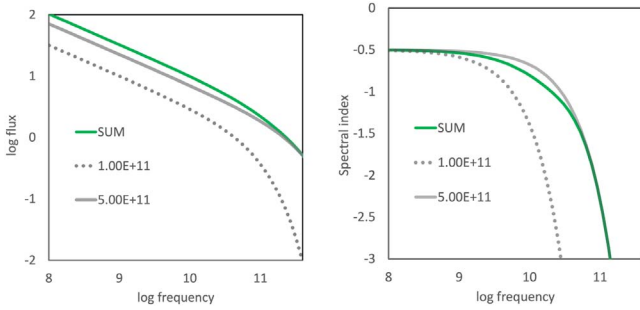
Figure 13. Spectra of two exponentially cut-off spectra in gray (each labeled with their cutoff frequency) and their sum, shown as green line here and in Figure 12. Left: log flux vs. log frequency. Right: spectral index as a function of log frequency. Note that each of the two gray curves maps to the same gray line in the color–color diagram, while their average maps to a different locus (green line in both plots).

Figure 14. Inferred magnetic field vectors after correction for Faraday rotation, superposed on the total intensity image. The lengths of the vectors are fixed; actual fractional polarizations in the northern lobe of 3C40B are ~10%, while the filaments are typically at least 50% polarized.

averaged over locally brighter regions; filled squares denote spectra that were recalculated by summing the fluxes in the individual MGCLS frequency channels and the LOFAR image. Their results are consistent within the errors.

For 3C40B, the flattest points scatter in a narrow region near the power-law line, suggesting a low-frequency spectral index of ≈−0.5. In regions where the spectra are curved, the shape of the spectrum from 3C40B is indistinguishable from that of the *E-fils*.

For comparison, we show three illustrative idealized spectral shapes, each with a low-frequency index of −0.5. The spectra are shown in Figure 13, while their color–color mapping is shown in Figure 12. The gray line represents an exponentially cutoff spectrum $S(\nu) = S_0 \left(\frac{\nu}{\nu_c}\right)^{\alpha} \times e^{-\left(\frac{\nu}{\nu_c}\right)}$, an approximation to the idealized spectrum of Jaffe & Perola (1973). This would result if the cutoff frequency were changing as a function of position in the source due to magnetic field changes, adiabatic changes, or radiative losses, but where the underlying spectral shape (relativistic electron distribution) remains the same. This idealized homogeneous spectrum falls off more rapidly than the data. In addition, we can rule out different power laws at different locations in the filaments, which would trace out the line of all power laws. Different power laws would have been expected in some scenarios where particle acceleration varied with distance from 3C40B.

There are many ways to broaden a spectrum, to move the locus in color–color space into the region between exponentially cut-off spectra and power laws, as is observed. We know, e.g., that there is more than one single spectral component along each line of sight from the different spectra of the narrow and broad components (Figure 10). The green line in Figures 12 and 13 represents the sum, at each position in the sky, of two exponentially cut-off spectra with cutoff frequencies that differ by a factor of 5. Then, at a fixed observing frequency, if the magnetic field were changing, e.g., the observed spectra would trace out the solid green locus in Figure 12. Alternatively, if the spectra do not shift with position along *E-fils*, but the spectrum with the high cutoff dominates the sum near the 3C40B jet, and the spectrum with the low cutoff dominates farther away, then this would follow a similar locus.

The green line accurately represents the spectral shape of the data. However, there are other ways to create this same shape as well. Instead of two exponentially cut-off populations with different cutoff frequencies along the line of sight, e.g., there
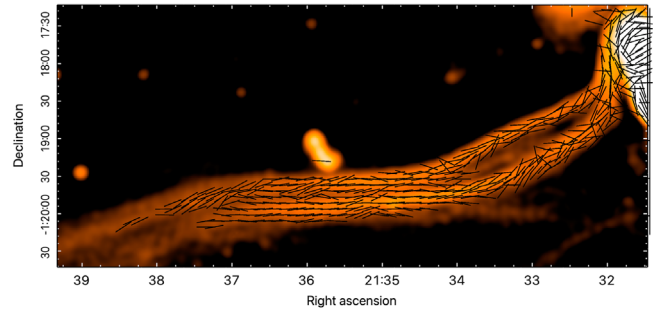
could be a single broader convex distribution resulting from particle acceleration. There could also be electron populations with different shapes at different positions in the source, embedded in their own respective magnetic field strength regions; these can still create what appears to be a simple locus in color–color space. In the discussion below, we do not attempt to identify a unique electron energy distribution for the jet and *E-fils*; we instead present physical scenarios that are compatible with the observations.

4.3. Pressure Estimation

Using the above values for the brightness and diameters of the filaments, we can obtain a rough estimate of their emissivities; combining these with the spectral index, we obtain an estimate of the minimum combined pressures of the cosmic rays and magnetic field (Brunetti et al. 1997). To calculate a first-order fiducial number, we assumed that the structures have a uniform emissivity (filling factor = 1), that the electron energies extend down to a somewhat arbitrary value ~300 MeV, and that the ratio of relativistic protons to electrons is 1 at a given energy. Using a position midway along the filaments, we made estimates for both the total emission and the individual filaments, used a spectral index of −1.6, and derived minimum pressures (=1/3 minimum energy density) of 1–2 × 10⁻¹² erg cm⁻³, corresponding to magnetic field values of ~7 μG. The actual pressures are likely to be higher, even by an order of magnitude or more, if the ratio of relativistic proton to electron ratio is 100, if the filling factor is smaller, if the electron distribution extends down to, e.g., 100 MeV, or if the ratio of magnetic field to cosmic-ray energy densities does not match these minimum conditions. These pressure estimates for the fields and relativistic particles in *E-fils* are used below to compare with those in the ambient medium, calculated from the X-rays.

4.4. Polarization

The peak amplitude in the cleaned Faraday spectrum at each pixel, along with its corresponding Faraday depth (RM) and phase, are used to map the polarized emission. A map of the *E-fils* and the adjacent northern section of 3C40B is shown in Figure 14. Where the S/N is sufficient, polarized emission is detected everywhere, except in isolated regions where a rapid change in angle causes local depolarization.

At the same positions as used in Figure 9, we sampled the 7″.75 maps in polarized flux, RM, and electric vector position angle corrected for the local RM. The resulting behavior of the
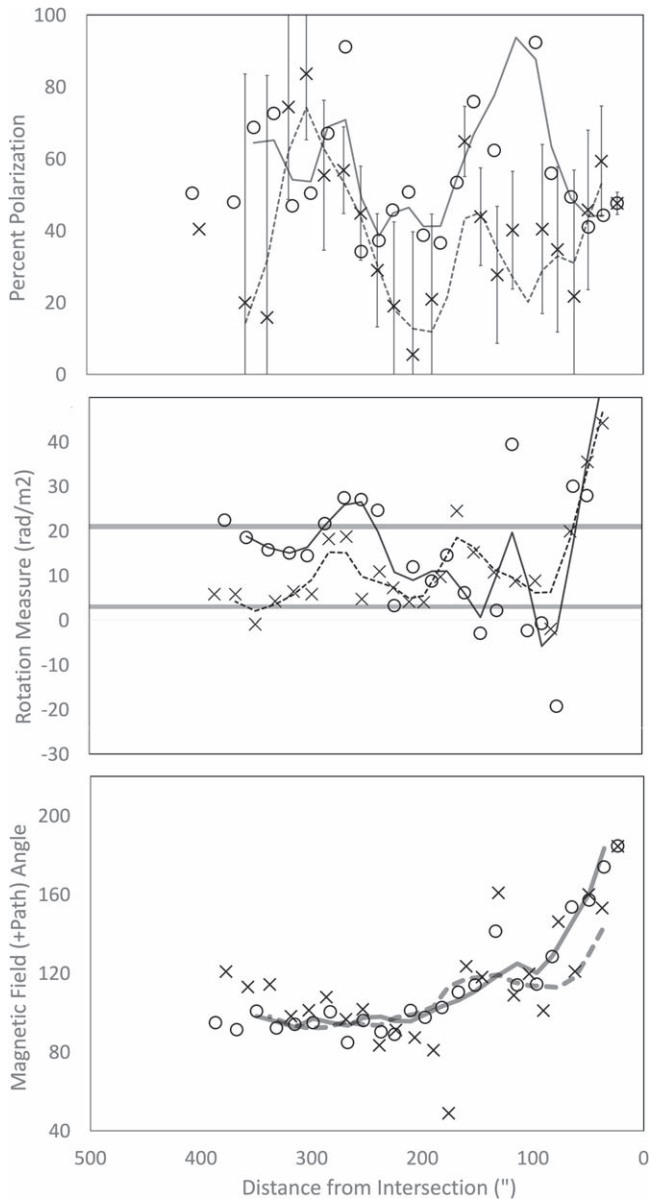
Figure 15. Polarization properties of the north (circles, solid line) and south (Xs, dashed line) filaments of *E-fils* as a function of distance from 3C40B. Top: percent polarization after correction for bias (errors shown only for south). Middle: peak RM. Lines are Hanning smoothed. Horizontal lines show the range of contributions from the Milky Way foreground. Bottom: inferred magnetic field orientation after RM correction. In the bottom panel, the lines (solid, north; dashed, south) are not derived from the polarization data; they indicate the local orientation of the filament.

Figure 16. Top two frames: 2D images of F(ϕ) in ϕ vs. R.A. space, i.e., the Faraday spectrum for the north and south filaments separately. The integrated flux in the Faraday spectrum is set to a constant at each R.A. Bottom: the *E-fils* region in total intensity at 7$''$75 resolution, aligned in R.A. with the top images. The yellow arrows indicate a feature discussed in the text.

polarization as a function of distance from 3C40B is shown in Figure 15. The fractional polarizations were calculated after correcting for the polarized flux noise bias.

There are several important findings from these measurements. First, the calculated percentage polarizations are high, with median values of 40% (50%) in the northern (southern) filament. The correction for the noise bias resulted in only 2 points out of 46 yielding negative percent polarizations, supporting the high median percentages, even in the presence of large uncertainties.

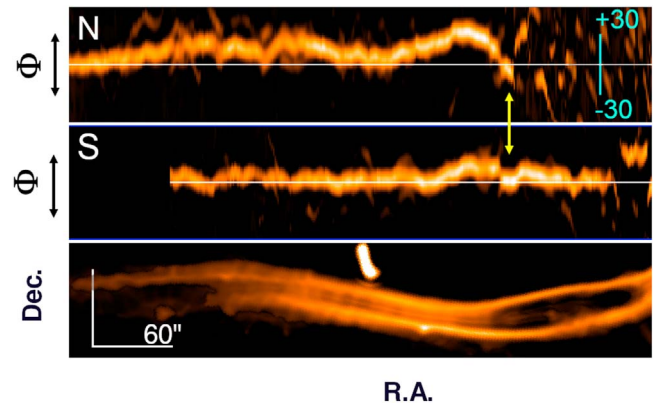Second, the rotation measures are found to lie within the narrow band corresponding to the local foreground RM from the Milky Way, so there is no detectable net RM from the cluster itself. They have an rms variation of only 9 rad m^{-2} along the filaments, similar to the variations across all the structures in the central region of A194 (see Figure 5); these variations are much smaller than seen in richer clusters. A considerably more detailed investigation of the Faraday structure is presented below.

Finally, the magnetic field direction is closely aligned, on average, with the local orientation of the filaments. The Faraday corrected magnetic field angles (based on the observed single dominant RM contribution), when smoothed, trace the orientation of the filaments as they range over $\sim$70$°$, mostly vertical at the intersection of *E-fils* with 3C40B, to nearly horizontal at large distances to the east (Figure 15).

To examine the Faraday structure of the filaments in more detail, we used a new implementation of Faraday synthesis (see Section 2 and W. Cotton & L. Rudnick 2022, in preparation), which achieves a Faraday resolution of 15.6 rad m^{-2}. We used $\nu \times Q(\nu)$ and $\nu \times U(\nu)$ to approximate the removal of the spectral dependence. The effect of not fully correcting for spectral index is that the peaks in Faraday space are broadened, while the mean Faraday depths remain unchanged.

The cleaned Faraday spectrum F(ϕ) at each pixel forms a cube, with axes corresponding to R.A., decl., and Faraday depth ϕ. From this cube, one can vary the position on the sky and extract an $F(\phi)$ versus position plane. To produce the F(ϕ) image in the ϕ versus R.A. plane, shown in Figure 16, we extracted the cleaned Faraday spectrum at each pixel in R.A. at the value of Dec corresponding to the ridge line of the filament. For each pixel in R.A., we then normalized the spectrum—for display purposes—so that the integrated polarized flux between Faraday depths of -40 rad m^{-2} and $+65$ rad m^{-2} was set to a constant value.

We briefly explore the type of information available in these R.A., decl., ϕ cubes. The common interpretation of Faraday structures is that they result from variations in the foreground plasmas that are not directly related to the source. The clearest exceptions to this are cases where the synchrotron structure and the Faraday structure are clearly related, e.g., cases of banding or draping (Guidetti et al. 2012, 2011; Müller et al. 2021, 2021). Rudnick & Blundell (2003) suggested that local effects might actually be a major contaminant to estimates of cluster magnetic fields, which are based on the assumption that they are unrelated foreground variations.

In A194, we are in the unusual position where the scatter in RM is quite low (see Figure 15 in Govoni et al. 2017), in contrast with rich clusters (e.g., Murgia et al. 2004). A more thorough discussion of A194's special nature is presented in Appendix B. With minimum confusion from foreground fluctuations, we suggest that the changes in Faraday depth, ϕ from pixel to pixel, can be mapped to distance along the line of sight. The 2D F(ϕ), ϕ versus R.A. images are then equivalent to a top view of the filaments, illuminating their 3D structure. This is perhaps best illustrated by its exception, where a foreground patch of ionized plasma likely creates a sharp jump in the Faraday depth in both filaments (the yellow line in Figure 16), with no corresponding structure in the plane of the sky. By contrast, most observed changes in Faraday depth appear associated with structures in the total intensity images.

Further discussions of isolating local Faraday effects from those of an unrelated foreground are found in Section 5.4 and in Appendix B. At this point, however, we note that neither the magnitude nor the sign of the scaling between Faraday depth (ϕ) and distance along the line of sight l are known. Since $\phi = n_e \boldsymbol{B} \cdot \boldsymbol{l}$, changing the direction of the magnetic field reverses the sign of the inferred change along the line of sight, while its magnitude scales with the electron density n_e and the projected magnetic field.

4.5. X-Rays

The X-ray surface brightness in the region of the *E-fils* was fit with a β-model plus an additional component for NGC 547 (which contributes very little at these distances). Pressures were calculated assuming a temperature of 2 keV, based on the kT map in Figure 6 of Bogdan et al. (2011) and normalizations based on a 4′ circle. At 2′.9 from NGC 547, at the western end of the *E-fils*, the density was 1.9×10^{-3} cm^{-3} with a corresponding pressure of 1.15×10^{-11} erg cm^{-3}. At the eastern end, 9′.6 from NGC 547, the corresponding values were 0.98×10^{-3} cm^{-3} and 0.6×10^{-11} erg cm^{-3}.

After removing detected point sources in the area, we extract a surface brightness profile along sectors of an annulus that extends from 5′ to 7′.5 from a center slightly north of the X-ray peak (R.A. 1:26:00, decl. −1:19:06). The sectors align with and cross the trajectory of *E-fils* (Figure 17). Surface brightness values are taken counterclockwise for each of the two bands separately, indicating a dip of the surface brightness in the location of *E-fils* (see Figure 18).

By adding the two subbands to construct a combined surface brightness profile from 0.4–3 keV and subtracting out a large-scale parabolic baseline, we identify a significant dip of $19 \pm 2\%$, spanning five sectors or ~1′.25 (27 kpc) at the location of *E-fils* (see Figure 18). The X-ray surface brightness dip extends somewhat beyond the radio emission, so for the purposes of calculation, we assumed an empty 35 kpc empty cylinder. With the nominal beta model, this would produce a dip of <10%. So if an empty cylinder is appropriate, then the line-of-sight distance through the cluster would have to be only 190 kpc, instead of the inferred 966 kpc ($2 \times R_{500}$). It is therefore possible that the X-ray emission has a flattened distribution along the line of sight; if this were true, then our estimates of the densities and pressures at the position of the *E-fils* would go up by ~$\sqrt{2}$. The brightness structure in the plane of the sky also indicates that the ICM is nonspherical, so a flattened distribution would not be surprising. In any case,
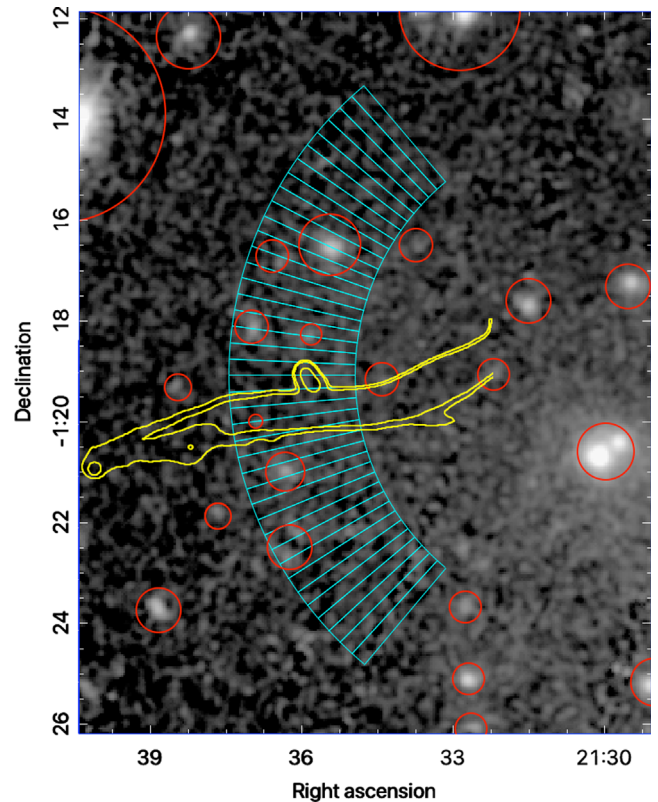

Figure 17. XMM-Newton image in a soft energy band (0.4–1.25 keV) with pixel size 2′′.5, and smoothed with a 3-pixel Gaussian. The cyan sectors are used to extract an azimuthal profile crossing the location of the *E-fils* (shown with yellow contours from the 15″ MeerKAT image). The X-ray sources circled in red are excluded from the analysis. The resulting surface brightness distribution is shown in Figure 18.

having at least a 35 kpc region that is completely empty of X-ray emitting material is difficult to avoid.

4.6. Closeup—the E-fils, North Jet Intersection

The narrow north and south filaments appear to merge and turn toward the north as they approach 3C40B, until they blend in with the brighter jet emission. This suggests that the two structures could be interacting. In this section, we examine the apparent interaction region.

We start by separating the different spectral components using the spectral tomography technique of Katz-Stone & Rudnick (1997). Since the *E-fils* have steeper spectra than the 3C40B jet, an image dominated by steep-spectrum material isolates them from the flatter jet-related emission.[15]

The results are shown in Figure 19. The key finding is that the steep-spectrum *E-fils* not only turn to the north as they approach 3C40B, but appear to wrap around the north end of this portion of its jet, as the jet abruptly bends to the west. In Section 5 we explore what can be learned about jet and filament physics from this apparent interaction.

---

[15] This involves taking two maps at different frequencies and subtracting the higher-frequency map from the lower-frequency map to yield ΔS_t with a scaling equivalent to an arbitrary spectral index α_t. In such a difference map, all structures with $\alpha = \alpha_t$ disappear, leaving positive residuals for regions with steeper α and negative residuals for flatter ones. To create the spectrally separated maps, we used the broadband 1283 MHz map (S_{1283}) and the corresponding spectral index map to create two pseudo-maps at the arbitrary frequencies of 850 MHz and 2000 MHz.
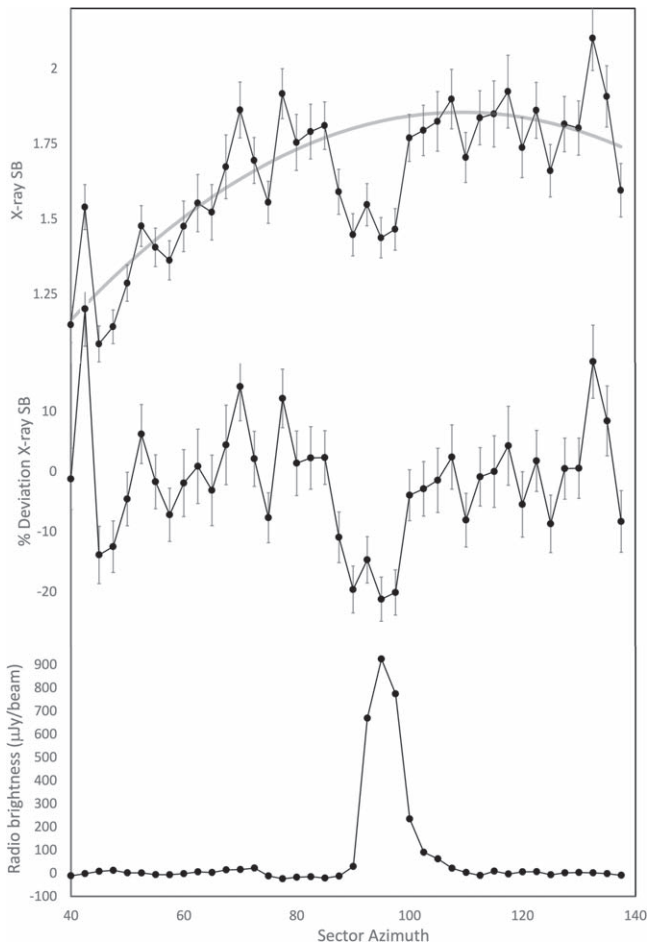
Figure 18. Top: X-ray surface brightness profile using the sectors in Figure 17 in units of counts/(ksec arcmin^2). The profile is made using the unsmoothed data that are shown (smoothed) in Figure 17. A second-order baseline is fit to the profile, ignoring the region of the dip, and is shown as a gray line. Middle: baseline-subtracted X-ray brightness in terms of percent deviation from the baseline. Bottom: radio profile from the 15″ MeerKAT image with a linear baseline subtracted. The emission from the compact background double just north of the filaments has been excluded. A dip of $19 \pm 2\%$ in the X-ray surface brightness is coincident with the peak in the radio.

Figure 19. Top: separation of steep-spectrum (red) and flat-spectrum (green) structures around the northern jet of 3C40B, constructed as described in text. $\Delta S_{0.5}$ in red, where most of the contribution from the flatter spectrum source 3C40B disappears, overlaid with the original 1283 MHz map in green. The red arrow indicates the apparent extension of the filaments to wrap around the top of a bend in the jet. Bottom: polarized intensity of the jet/filament interaction region color-coded by RM, as shown in the color scale.

There is also a dramatic shift in the Faraday structure at this point, as shown in Figure 19. Where the *E-fils* and 3C40B intersect, the peak RM jumps by $\sim$30 rad m^{-2}; adjacent to this is a depolarized region of 3C40B and some hint that higher RMs are also found in the jet at this point.

To examine this transition more carefully, we again turn to the high resolution version of the Faraday spectrum, this time correcting for an effective spectral index of -0.5, since we are primarily interested in the flat-spectrum northern jet of 3C40B. Figure 20 shows the Faraday depth versus R.A. plane at fixed decl.; as in Figure 16, this is equivalent to a top view if we interpret the Faraday depth as a distance along the line of sight.

The most important conclusion from this display is that the northern segment of the jet (between points C and D) has a smooth gradient in Faraday depth that connects directly to the Faraday depth of the *E-fils* —there is no sudden jump at the *E-fils,* as one might conclude from a superficial look at the peak RM distribution shown in Figure 19. In retrospect, one can see the same gradient in Figure 19, while Figure 20 makes it much more obvious. If we now interpret the Faraday depth changes as line-of-sight changes, then the jet from locations C to D
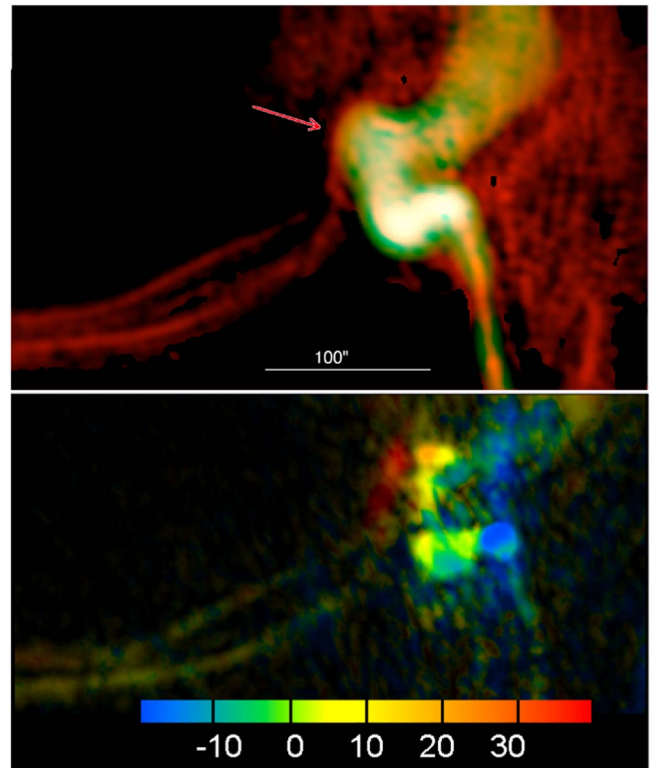
meets up with *E-fils* along the line of sight, just as they meet up in the plane of the sky. This confirms that the jet and *E-fils* are indeed interacting and are not simply superposed in the plane of the sky.

Note also that there is a change in the 3C40B jet at point D, where it bends by 45° to head NW into the much more diffuse faint northern lobe. At this same position, the trend in Faraday depth reverses, showing that this is a change in 3D, not simply in the plane of the sky. The correspondence between the changes in trajectory in the plane and in Faraday depth would be an (unlikely) coincidence if it were due to an unrelated foreground screen; this provides additional support for the line-of-sight interpretation of Faraday depth in this system.

The connection between Faraday depth and distance provides a new tool for estimating the magnetic field strength in the ICM. If we make the reasonable assumption that the orientation of the jet between C and D is at 45° to the line of sight, then the linear distance of 18 kpc between C and D corresponds to a change in Faraday depth of $\sim$40 rad m^{-2}. Using the density of 1.9×10^{-3} cm^{-3} from the X-rays yields a magnitude of 1.4 μG for the component of the magnetic field along the line of sight.

This is the first estimate of magnetic field strength from a single region of Faraday-rotating material in a cluster ICM. Previous estimates are based on the statistical properties of RM fluctuations, scale sizes, and variations in field strength and densities over the cluster. Our single-region estimate is, of course, uncertain by factors of order unity because of unknown projection effects for both the jet and the magnetic field
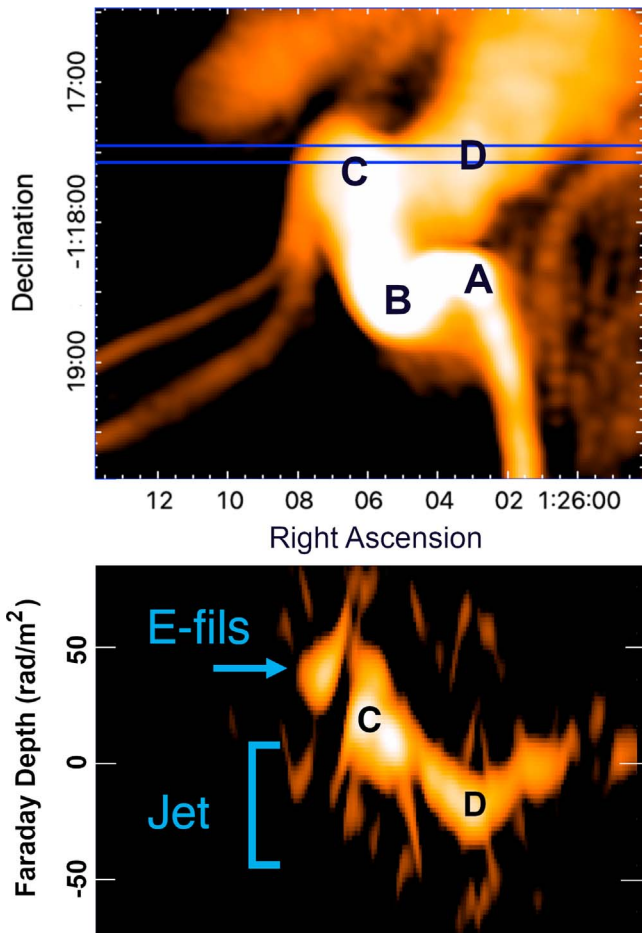
Figure 20. Top: MeerKAT total intensity of 3C40B in the region of the interaction with the *E-fils*. Letters mark the locations of bends in the jet. Bottom: polarized intensity produced by the high resolution cleaned Faraday spectrum. Plotted in the Faraday depth vs. R.A. plane, at the fixed decl. marked by dark blue lines in the top panel. The cyan arrow shows the polarized emission from the *E-fils*, while the rest of the emission is from the jet.

orientation. The value of $1.4\,\mu G$ for the surrounding ICM is a factor of 4 below the minimum pressure magnetic field of $5.8\,\mu G$ calculated for the portion of the jet between points C and D, using the observed spectral index of -0.52 and the same assumptions as used for the filaments above.

4.7. X-Rays in the Northern Jet

The XMM-Newton observation shows an X-ray source at the location of the intersection of the northern jet with *E-fils* (Figure 21). There is no hint of any extent in the XMM-Newton images. This X-ray source is also seen in the Chandra observation (OBSID 7823, 65ks) at the edge of the ACIS S2 (ccd_id = 6) during an observation of A194 centered on ACIS-S3. Using the Chandra point-spread function (PSF) calculator for the off-axis location, at the very edge of the field of view (FOV), the source is also consistent with a point source with an FWHM = $2\rlap{.}{''}5$. Hence, we refer to this X-ray emission as an unresolved X-ray feature (UXF). It is possible that the X-ray and radio superposition is random; it is difficult to estimate this probability a posteriori. Still, the X-ray source density is low, and a random alignment on such a unique location of the radio structure seems small.

The UXF is listed in the compilation of X-ray sources in the field of A 194 by Hudaverdi et al. (2006). There are a number
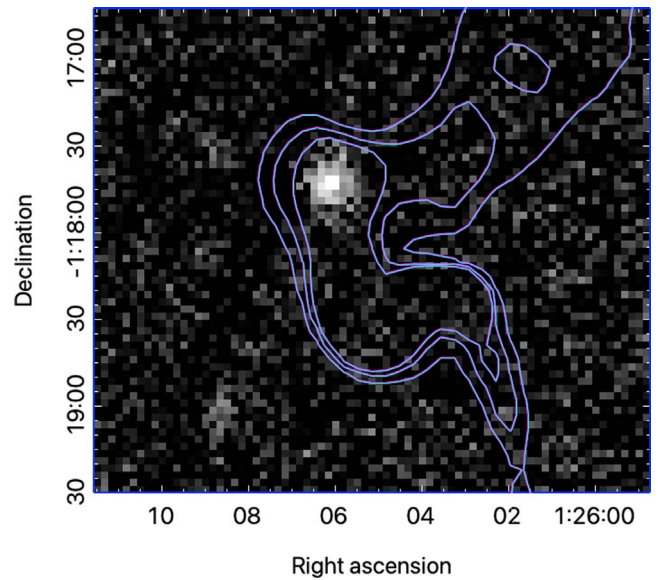
Figure 21. X-ray XMM EPIC image overlaid with total intensity contours of the northern jet of 3C40B.

of other X-ray sources coincident with faint, compact radio sources in the field. Hudaverdi et al. (2006) note a large excess of compact X-ray sources in this field, which they attribute to the fueling of AGN during cluster infall. However, except for the UXF and the X-ray sources that are associated with NGC 541, 545, and 547, none have any apparent connection to the radio structures 3C40B and 3C40A or the accompanying filamentary features.

The XMM-Newton spectrum of the UXF is consistent with both a power law (spectral index 2.15 ± 0.12), and a thermal model with a temperature of $1.84 \pm 0.28\,keV$ and a low abundance of $Z = 0.17 \pm 0.12\,Z_\odot$. The model-predicted (unabsorbed) flux is $2.8 \times 10^{-14}\,erg\,s^{-1}\,cm^{-2}$ in the 0.5 to 2 keV band. Assuming the X-ray emission is associated with a cloud of thermal gas with the size of the Chandra PSF ($\sim 1\,kpc$), the gas mass is about $5 \times 10^6\,M_\odot$.

We found no evidence for a counterpart to UXF in SDSS u, g, i, r, or z images or in the near- or far-UV images from GALEX. There is a very faint apparent source at this location in the unWISE W1 co-adds, although the background density at this brightness means the probability is high for a spurious detection.

5. Discussion

The following section addresses the origin of the *E-fils*, the ways in which they interact with the radio jet/ICM, and the implications for relativistic particle (re-)acceleration. We briefly summarize below the key points from this section to provide a framework for the more detailed discussions. In our concluding remarks, we emphasize the more general and important implications of this work for the relativistic particles and fields and thermal plasmas in groups and clusters of galaxies.

5.1. Key Points

1. Magnetized filaments, composed of bundles of smaller fibers, arise naturally in turbulent magnetic plasmas and

will reflect the eddy turnover lengths and times of the driving forces.

2. Filaments will be be further stretched, and their magnetic fields amplified, by bulk motions in the ICM and by encounters with radio jets.

3. Magnetic pressures in filaments can reach significant fractions of the ambient thermal pressures, and together with accompanying cosmic rays, can plausibly expel the local thermal plasma.

4. A scenario in which a dense moving cloud encounters the northern jet of 3C40B, bending it and the *E-fils*, appears plausible.

5. Either streaming of cosmic-ray electrons from a radio galaxy, or, more likely, the (re-)acceleration of seed electrons from the ICM through betatron or other mechanisms, is required to illuminate the filaments.

5.2. The Ubiquity of Synchrotron Filaments

Long, thin, synchrotron-emitting filaments are becoming ubiquitous in radio maps of sufficient resolution and sensitivity. They are found in peripheral radio relics, e.g., A2256 and A3376 (Owen et al. 2014; de Gasperin et al. 2022) and as polarized features e.g., in A2255 and MACS J0717.5 + 3745, which are likely peripheral, but projected onto the cluster interior (Pizzo et al. 2011; Rajpurohit et al. 2022a). They are found in the neighborhood of radio galaxies (Ramatsoku et al. 2020; Brienza et al. 2022) and even inside radio lobes, e.g., Centaurus A (Wykes et al. 2014) or M87 (Hines et al. 1989). Sometimes, these filaments connect old tails of radio galaxies to diffuse radio emission (de Gasperin et al. 2017; Wilber et al. 2018; Botteon et al. 2020; Mandal et al. 2020). Possibly analogous complex and extended synchrotron structures include those in the wake of radio galaxy NGC1272 in the Perseus cluster (Gendron-Marsolais et al. 2021). Synchrotron filaments are also prominent in the Galactic Center region (Yusef-Zadeh et al. 2021) and in supernova remnants (Milne 1995). Given the wide variety of physical conditions in these environments, it becomes clear that filament formation is a natural result of dynamic magnetized astrophysical plasmas.

In A194, we see a rich network of filaments, shown in more detail in Appendix A. Many of these appear associated with the luminous radio galaxies 3C40A and 3C40B. The most prominent filaments are the *E-fils*, which are the subject of this paper. Consideration of the observational findings listed above and the filamentary magnetic structures seen in MHD simulations lead us to a preferred origin scenario. In this scenario, the *E-fils* are initially generated by shear flows in the A194 cluster, followed by interactions with the 3C40N jet and a dense ICM clump, which stretch and amplify the filaments and lead to the reacceleration of the embedded cosmic-ray electrons.

5.3. Shear and the Generation of Filamentary Magnetic Bundles

Simulations show that extended bundles of magnetic fields are ubiquitous in turbulent MHD flows in high-β environments, where transverse magnetic field pressure gradients can be balanced by ambient pressure gradients (e.g., Porter et al. 2015). The strongest fields tend to be substantially stronger than the global mean field and are separated into distinct bundles of fibers with lengths reflecting the driving scales of the local turbulent flow (Porter et al. 2015; Vazza et al. 2018). The individual thicknesses of the fibers are set by the limiting transverse resistivity scales, so are likely smaller than a kiloparsec (Zhuravleva et al. 2019). The apparent ∼3 kpc filament thickness of the narrow component radio filaments is then not the physical width of an individual magnetic fiber, but more likely the width of a bundle of illuminated aligned fibers, held together by the tension along the field lines. More broadly distributed ensembles of weaker fiber structures could then be responsible for the even broader component of *E-fils*.

Magnetohydrodynamics simulations have demonstrated that magnetic folds that occur in a turbulent dynamo succumb to tearing at high Reynolds numbers, leading to increasingly longer field structures. In general, such studies show that when the seed magnetic field for a turbulent dynamo is weak, then the amplified magnetic energy initially peaks at the small, resistivity-based scales. This proceeds until the developing magnetic field becomes strong enough by stretching that the back-reaction on the small-scale ambient turbulent dynamical stresses becomes significant (see, e.g., Schekochihin & Cowley 2007, for a review and Galishnikova et al. 2022).

Subsequently, thin current sheets are torn into fiber bundles that extend to increasingly larger scales via stretching, until at saturation, the magnetic stresses become comparable to the fluid dynamical stresses on turbulence-driving scales. Then, the longest filamentary magnetic structures approach a substantial fraction of that driving scale. When this turbulence is driven by highly nonisotropic dynamics, such as we may expect in merging clusters, these filament lengths would reflect the scales associated with the active drivers, which can extend to cluster scales (e.g., Vazza et al. 2018).

If the magnetic fields have indeed been amplified by shear stretching, as described above, we expect the field strengths to scale as $\rho v^2/\ell$, where ρ is the density of the turbulent plasma, with a characteristic velocity v on the driving scale ℓ. For a turbulent Mach number of order $1/2$, as commonly assumed for ICMs, the maximum magnetic pressures would then be several times lower than the ICM pressure (e.g., Porter et al. 2015; Miniati & Beresnyak 2015). This is what the observations suggest for the *E-fils*.

In the low-mass system A194, the field stretching is likely dominated by the large-scale bulk flows from continuing infall suggested by the motions of NGC 545 and NGC 541 with respect to the X-ray medium centered on NGC 547 (Bogdan et al. 2011). Bogdan et al. (2011) use inferred pressures in the galaxies to show that their velocities in the plane of the sky are about 800 km s^{-1} for NGC 541,5, while their radial velocities are <100 km s^{-1} with respect to the cluster. The infall of these galaxies and any accompanying gas would thus be primarily from the west. The >200 kpc long gently curved *E-fils* structure, with its high fractional polarization and aligned magnetic field, is consistent with this picture of flow-induced stretching. The lack of strong, much smaller scale (10 s kpc) RM variations that are seen by contrast in rich merging clusters again indicates the dominant role of stretching by large-scale bulk motions in A194, instead of by smaller-scale turbulence.

Whether or not this picture is viable depends on the lifetimes of the filaments. The dynamical lifetime of a filament of length L, formed in a sheared flow pattern with characteristic velocity
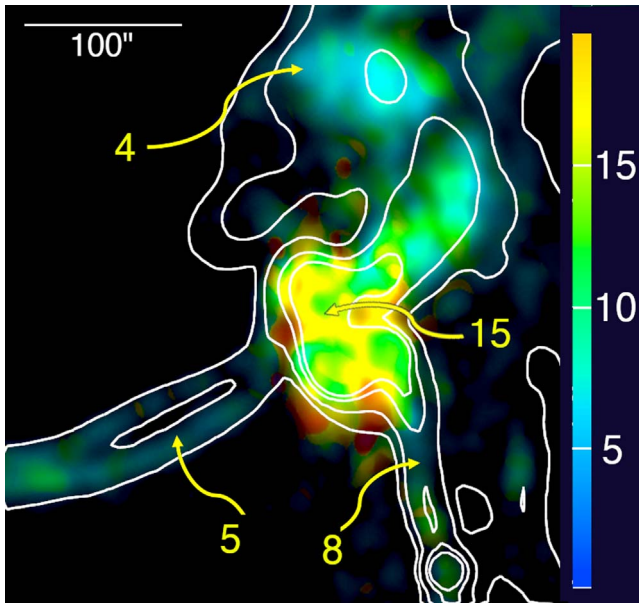
Figure 22. Map of the rms width of the high resolution Faraday spectrum at 15″ resolution, with an assumed spectral index of -0.5 . The color bar and numbers for different regions are in units of rad m^{-2}. The rms width is an indicator of multiple Faraday depths along each respective line of sight; any value below six is essentially unresolved in Faraday space. The intensity and contours are from the total intensity image.

v, is set roughly by

$$\frac{L}{v} \sim \frac{L}{(M \cdot c_s)} \sim \frac{200 \text{ kpc}}{(M \cdot 1000 \text{ km s}^{-1})} \sim \frac{200}{M} \text{ Myr.}$$

$M < 1$ is the turbulent Mach number, and c_s is the sound speed. This is likely comparable to the synchrotron lifetimes in the absence of a resupply of cosmic-ray electrons into the high field regions (see Section 5.5). Therefore, this overall scheme appears plausible to explain observed filaments. It also implies that additional weaker magnetic field bundles are likely to intermittently thread the entire cluster volume and become lit up above current detection limits once a sufficient population of high-energy cosmic rays is locally accelerated.

The discussion above does not explain the changes in structure or spectra of the filaments as a function of distance from 3C40B. For this, we need to examine the region where the E-fils and 3C40B's northern jet appear to interact, as we do in Section 5.4.

5.4. Jet-Filament-ICM Interactions

The northern jet of 3C40B goes through a series of sharp bends, both as projected onto the plane of the sky and along the line of sight (Figure 20). These bends are not mirrored in the southern jet, and are thus unlikely to be the result of jet precession (e.g., Ekers et al. 1978) or displacement due to orbital motions (e.g., Lupton & Gott 1982). The remaining alternative is that the jet interacts with a clump of higher-density ICM material, causing one or more of the observed bends.

Figure 22 provides evidence from Faraday rotation that the thermal plasma in the region of the bends is indeed denser than elsewhere along the jet. The dramatic increase in the width of the Faraday spectrum near the bends suggests a denser environment that is likely mixed, on either microscopic or

macroscopic scales, with the synchrotron-emitting plasma. The UXF at the top bend in the jet (Figure 21) may be another indication of local dense thermal material, though its origin remains unclear.

Turning now to the E-fils, their largely east–west structure appears to curve north and drape over the final sharp bend in the jet (Figure 19). Along the E-fils, the narrow filaments are stronger than the broad component as they approach the jet (Figure 8), accompanied by an overall flattening of the spectral index (Figure 9). These systematic changes would not arise naturally from only the shear motions discussed above, which do not depend on the jet. We thus need to investigate how the jet, E-fils, and a high-density clump in the ICM could mutually interact.

5.4.1. Filament Stretching and Magnetic Field Amplification

A filament embedded in a shear flow will be stretched, as long as the tension stress from the field (roughly the magnetic pressure divided by the length over which it is being stretched) is weaker than the flow-based, dynamical stretching force. The field strength then increases in proportion to the increased filament length. The strongest filament fields built from ICM-based flows are limited because within subsonic ICM flows, the local plasma β values will remain significantly greater than unity, while flow speeds are generally subsonic. In strong flows with major transitions (e.g., the flow around an advancing jet), the lengths and field intensities can increase by factors of a few.

We observe gentle bends in the E-fils ($\sim$15° and $\sim$22° at 100 kpc and 50 kpc from the jet, respectively). A much sharper bend of $\sim$60° to the north is seen at $\sim$7 kpc ; this strongly indicates an interaction with the jet. Using simple geometry, we can estimate the amount of stretching associated with these bends— for the gentle bends it is $\leqslant$16%, but for the large bend near point C (Figure 20), the E-fils have likely been stretched locally by a factor of $\sim$3, from $\sim$16 to $\sim$46 kpc. This is a likely explanation for the relatively brighter narrow components of E-fils closer to the jet (Figure 8). However, because the narrow components appear enhanced out to $\sim$250″ from the jet, an additional source of stretching from the ICM is required in the direction away from the jet and cluster center.

The above discussion assumes for simplicity that the stretching happens only in the plane of the sky. The E-fils likely also stretch along the line of sight, increasing the total amplification of the magnetic field.

5.4.2. Interaction Scenarios

In addition to stretching the E-fils as they encounter the jet and drape over it, we must account for the bending of the jet itself. As shown above, this likely involves some denser region of the ICM. Figure 23 depicts three possible scenarios for this three-way interaction. In Scenario I (top panel), we assume that the filament is broad enough and has enough magnetic tension to deflect or retard the jet during the encounter, and the dense ICM is simply swept up by the jet. In Scenario II (middle), the jet hits a stationary cloud that is intersected by the magnetic filament. Upon impact, the jet is deflected by the dense cloud. Momentum is imparted onto the cloud, which is then displaced, dragging the magnetic filament with it. In Scenario III (bottom), the propagating jet interacts with a moving cloud that crosses its path, generating a complex interaction. The E-fils are dragged by the subsequent motions in the ICM. For
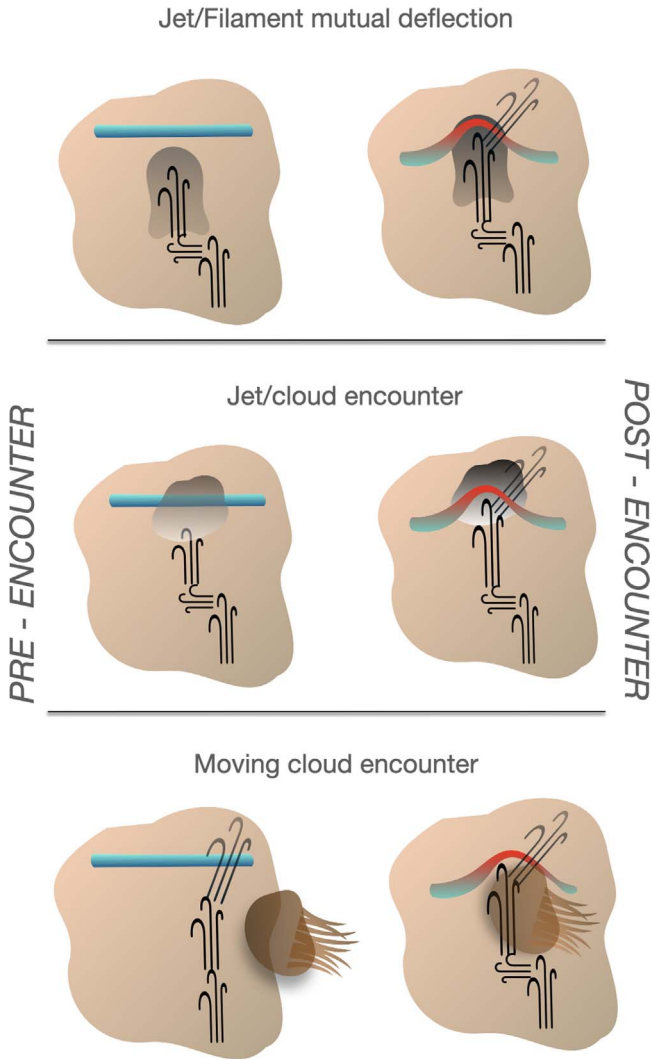
Jet/Filament mutual deflection

PRE - ENCOUNTER

POST - ENCOUNTER

Jet/cloud encounter

Moving cloud encounter

Figure 23. Three possible scenarios for the interaction of 3C40B's jet (represented by the line triplets) with the *E-fils*. In the text, these are referred to as Scenarios I (top), II (middle), and III (bottom, preferred).

reasons discussed below, we believe that Scenario III is the most likely.

5.4.3. Bending the Jet

We begin by examining Scenario I. For the magnetic tension in the filament to deflect the incoming jet, the fields will need to be amplified until they become dynamically significant. If the tension force ($\propto B^2/l$, where l is the length over which the filament stretching is concentrated) were comparable to the jet ram pressure, ρv_{jet}^2, then the work to stretch the filament could play a significant role. To place this in context, if the fields near the interaction point were, for example, amplified by a factor of 3, then the tension force could be enhanced by nearly an order of magnitude over analogous tension forces from this filament. However, if the jet is internally supersonic, the momentum flux in the jet will be dominated by the ram pressure ρv_j^2 of the jet material rather than internal pressure in the jet, which is often assumed to be in pressure equilibrium with the ICM. In this case, even if the filament plasma beta $\beta_p = 8\pi P_{gas}/B^2$. approaches unity, the momentum flux from the kinetic jet will dominate the external tension force. This means that the jet material will not be deflected significantly by interaction with

the draped filament; this effectively rules out Scenario I. In addition, this scenario provides no explanation for the earlier bends in the jet.

Scenario II implies the presence of a dense cloud that acts to deflect the jet at point C in Figure 20. The Faraday structure, in fact, suggests increased amounts of thermal material in this area (Figure 22). The impact of the jet onto this cloud imparts momentum to the cloud. The magnetic filaments appear to pass through or near the cloud, so the filaments are then carried along, draped over the cloud. However, such a cloud will not act as a solid body. As jet momentum is deposited in the cloud, the outer portions of the cloud will be stripped away while the core of the cloud may acquire some bulk recoil velocity v_c. Simulations would likely be necessary to fully determine the relation between an effective recoil velocity, the density ratio of the cloud and the jet material (ρ_c/ρ_j), and the jet velocity (v_j).

The main difference between Scenarios II and III is the motion of the dense cloud. In Scenario II, the jet must bend sharply by other means prior to the cloud encounter, such as encounters with additional, otherwise invisible dense clumps, while in Scenario III, the multiple bends in the jet trajectory are a result of the encounter itself (Nolting et al. 2022). Consideration of the timescales associated with the jet evolution and cloud motion can help establish which of these options is more attractive. If the cloud motion is significant during the evolution of the radio jet structure, then we must reject Scenario II. Recent simulations (Nolting et al. 2022) show that such interactions strongly alter the character of the jet even during the early phases of an encounter when the jet impacts onto the less dense outer regions of the cloud, so we base our timescale on the half-jet-crossing time. If the cloud is assumed to be in orbit in the cluster, it will likely have a velocity of a few 10% of the sound speed. If the cluster temperature is 1.4 keV, then the sound speed is close to 600 km sec^{-1}. With an estimate of the cloud velocity (taken here to be $v_c \sim 200$ km s^{-1}) and the width of the jet (barely resolved diameter of 2.8 kpc), we find that the time for the cloud to cross half the width of the jet is on the order of 7 Myr.

Then, we consider the time required for the head of the jet to advance through the ICM. Analytical calculations (Nolting et al. 2019) show that the Mach number of the propagation of the head of the jet through the ICM, M_h, will be lower than the internal Mach number of the jet, $M_j = v_j/c_{s,j}$, where $c_{s,j}$ is the sound speed in the jet. Simulations show $M_h \sim 0.7M_j$. These radio jets are expected to be supersonic, with internal Mach numbers of a few. Assuming $M_j > 2$, then the distance between point A and point C (about 25 kpc projected) yields an estimate of ~ 30 Myr for the interaction time. Since the time for the head of the jet to move over the extent of the cloud (30 Myr) is much longer than that for a typical cloud to cross the jet (7 Myr), the moving cloud scenario is favored. In addition, the intersection with a moving cloud will cause multiple bends in the jet. We therefore adopt Scenario III as the most likely option.

Nolting et al. (2022) shows a simulation of such a jet-cloud encounter (including an animation in the online journal version), including the multiple resulting bends in the radio jet. The initial glancing deflection could explain emission at point C in 3C40B, while the jet propagation prior to the encounter explains the trajectory beyond point D. Since the deflection at point A is approximately 90°, there must be a dense core in the cloud near the midpoint of the jet to abruptly reorient the jet. Finally, the deflection of the jet causes it to

intersect with the *E-fils,*, whereas it previously passed in front or behind them. Subsequently, ram pressure from the jet and the moving cloud bends and stretches the filaments. In this way, Scenario III naturally explains the multiple sharp bends in the jet given the relative timescales for jet advance and cloud motion. The presence of the cloud is not ad hoc because it is supported by the increased Faraday depths in the interaction region. In this and any of the scenarios, the presence of the *E-fils* at the interaction point appears fortuitous. However, if the interaction resulted in the brightening of the *E-fils*, then we would identify them precisely because of this fortuitous interaction.

5.5. Cosmic-Rays

Synchrotron emission in clusters is found in radio galaxies, where the cosmic-ray electrons are initially ejected at the AGN, and in diffuse sources such as halos and relics, where more distributed sources of cosmic-ray electrons must be invoked. Filaments provide an interesting intermediate case, where the origin and evolution of their cosmic-ray electron populations have not yet been addressed. The *E-fils*, along with the other filaments in A194, present an opportunity to explore the possibilities, as we do in the following. The discussion is organized as follows: Section 5.5.1 explores the possibility that 3C40B is the source of the electrons; in Section 5.5.2 we provide an overview of the origin of cosmic-ray electrons in the ICM, with Section 5.5.3 then describing a scenario in which cosmic-ray electrons from the ICM are accelerated in the *E-fils*. Diffusion of electrons from the filaments is addressed in Section 5.5.4, and, finally, we discuss in Section 5.5.5 what can be learned from the observed shape of the *E-fils* synchrotron spectrum.

5.5.1. 3C40B as a Source of E-fils Cosmic-Rays

We now consider whether the radio galaxy 3C40B itself could be the source of the electrons associated with the *E-fils*, invoking streaming along the magnetic field. Modeled via pitch-angle scattering, electrons diffusing along field lines in a time, t, cover a distance $d \sim 2\sqrt{D_{||} t}$ where the diffusion coefficient along the field lines is $D_{||} \sim 1/3(c^2/\nu_s)$. In this expression, $\nu_s = \tau_s^{-1}$ is the electron pitch-angle scattering rate determined by resonant and nonresonant coupling with kinetic-scale electromagnetic fluctuations in the vicinity of the magnetic filament. One major challenge to this possibility is the need for diffusion to be sufficiently fast; that is, electron scattering rates that are slow enough for electrons to propagate at least ~200 kpc along filaments on a timescale that is shorter than or comparable to their radiative cooling time ($\tau_{rad} \sim 100$ Myr). This would imply strongly super-Alfvénic streaming along the filaments with a lower limit on the effective scattering timescale $\tau_s \sim 10^4$ yr.

Streaming electrons from 3C40B could also account for the presence of the diffuse steep-spectrum component surrounding the narrow filaments in the *E-fils*. The diffuse component could be generated by electron diffusion perpendicular to the local mean field; under conditions typical of the ICM, electrons may undergo a super-diffusive process up to the Alfvén scale (Xu & Lazarian 2022, and references therein,) spreading out on $L_{perp} \sim 10–100$ kpc while they are diffusing along the field lines.

In order for the jet to be the source of electrons for the *E-fils*, the two bright narrow components would need to reconnect with the field of the radio galaxy. This could happen through the relative motions between the jet and the turbulent ICM. In turbulent reconnection theories, the reconnection rate (generally defined by the inflow speed of field lines into a reconnection site) is fairly independent of the plasma resistivity and may reach a significant fraction of the local Alfvén speed (e.g., Lazarian & Vishniac 1999). Here the local Alfvén speed could be a substantial fraction of the ICM sound speed. This reconnection modifies the local magnetic field topology and could establish an effective electron transport channel between the radio galaxy lobe/jet and the external ICM. If magnetic reconnection between radio galaxies and ICM magnetic filaments is happening in A194, this could explain why the filaments are seen so prominently between and near the radio galaxies and are not more broadly distributed throughout the ICM, as traced by the X-ray emission.

Interestingly, this scenario could at the same time explain the increase in the ratio of brightness between diffuse steep-spectrum emission and the filamentary emission with increasing distance from the radio galaxy.

5.5.2. Cosmic-Rays in the ICM

Relativistic electrons are injected into the ICM by shocks, galactic winds, and AGN (e.g., Brunetti & Jones 2014, for a review, including the alternative mechanism of producing electrons through cosmic-ray/thermal interactions). These electrons have a maximum lifetime in the ICM, $\tau_l \gtrsim$ Gyr, at energies around 100–300 MeV. The lifetime decreases both toward higher energies ($\tau_l \propto E^{-1}$) due to radiative (synchrotron and inverse Compton IC) losses, and toward lower energies ($\tau_l \propto E$) due to Coulomb losses (e.g., Sarazin 1999). The long-lived electrons are advected and distributed on large scales by complex gas motions in the ICM, and constitute a nonthermal component that is effectively mixed with the ICM.

This nonthermal component can be reaccelerated to higher energies ($\geqslant$several GeV) through turbulence and shocks generated within the volume of massive clusters. This is especially true during mergers and through accretion of matter from connecting cosmic filaments. Turbulence is expected not only in massive clusters, but also in less massive systems and galaxy groups (Vazza et al. 2006; Nagai et al. 2013)

In relatively relaxed ICM and in the less massive systems, low-level turbulent electron reacceleration and adiabatic compression resulting from cosmic accretion inflows could balance radiative losses sufficiently to maintain the energy of relativistic electrons at several 100 MeV for times comparable to the cluster lifetime. In this minimum-maintenance situation, synchrotron radiation is expected at ultra-low frequencies, below those accessible to observations. However, even then, localized regions with stronger turbulent energy fluxes, so more effective electron reacceleration and stronger magnetic field amplification, could produce synchrotron emissions at higher frequencies. Filamentary structures with steep synchrotron spectra would be a signature of these localized acceleration/amplification regions, working on the pool of ~100 MeV minimum-maintenance electrons. If radio halos are observed at >100 MHz frequencies, then a background source of higher-energy electrons already exists and could feed into more localized filamentary structures. The very faint diffuse emission south of the *E-fils* (Figure 6) suggests the existence of a vast

reservoir of seed electrons in A194. Whether or not this is viable could be tested by deeper low-frequency observations of the structure and spectra of the diffuse emission.

5.5.3. Acceleration in Filaments

Assuming a background population of $\geqslant 100$ MeV electrons, they will encounter regions where a turbulent magnetic field is stretched and amplified by shear motions and radio galaxy interactions. The electrons spiraling in such an amplifying magnetic fields with $\dot{B} > 0$ are subject to an electromotive force and can consequently be (re)accelerated, e.g., via the betatron mechanism (see Melrose 1980, for a review). In the simplest applicable case where the magnetic field grows on a timescale shorter than the cooling time of electrons, while electron pitch-angle isotropy is preserved by scattering, the energy increment of the electrons in this case is $(\Delta pc)^2 \sim (2/3)(pc)^2 \delta B/B = (2/3)(pc)^2 \phi$, with $\phi = \delta B/B$.

The combination of the increase of both the magnetic field strength by a factor $\phi > 1$ and electron energy leads to a relative increase in characteristic synchrotron emission frequency, $\nu_s/\nu_{s0} \sim (1 + 2/3\phi)(1 + \phi) \sim (1 + \phi)^2 \sim \phi^2$, where ν_{s0} is the characteristic frequency prior to the field enhancement. This behavior could lead to the development of distinctive, steep-spectrum synchrotron emissions in the 100–1000 MHz range from the strongest ICM-turbulence-generated filaments as they interact with large-scale shear motions and/or radio galaxy jets. This would depend on the presence of magnetic fibers strong enough prior to the amplification that radio emission at ultra-low radio frequencies was already present and sustained at modest levels by reacceleration in the turbulent ICM.

The field stretching that occurs in the *E-fils* is strongest near the encounter with the 3C40B jet, as discussed above. The electron acceleration rate would thus rise strongly closer to the jet, and could at least qualitatively account for the brighter narrow filaments and flatter spectral indices there (Figures 8 and 9).

5.5.4. Diffusion of Cosmic-Rays from Magnetic Filaments

In addition to the possibility of diffusion along the *E-fils* with its aligned magnetic fields, energetic electrons could diffuse perpendicular to the filaments. This diffusion might be responsible for the broad component of *E-fils* in which the narrower filaments are embedded.

Electrons propagating along turbulent magnetic field lines on scales $\leqslant l_A$ (where l_A is the Alfvén scale, i.e., the scale where the turbulent velocity equals the Alfvén speed) can effectively exhibit super-linear diffusion in the direction perpendicular to the local mean field due to fast field line wandering. This may sometimes lead to an effective transverse diffusion rate that is comparable to that of pitch-angle-mediated particle diffusion parallel to the mean field (see, e.g., Lazarian & Xu 2021).

In such scenarios, electrons accelerated within the stretching field filaments could diffuse into the surrounding region where the magnetic field is lower. There, emissions at a given frequency would come from more energetic components of the electron spectrum that are more impacted by radiation energy losses. The associated electron energy spectrum would then be steeper, consistent with the observed steeper synchrotron component. Such diffusion might even be responsible for the

diffuse component filling the space between 3C40A and 3C40B (Figure 6), or the faint emission south of the *E-fils*.

5.5.5. The Energy Distribution of Filament Cosmic-Rays

In Figure 12 we showed that the observed spectra are significantly broader than and inconsistent with a simple exponentially cutoff spectrum. A broadening like this would occur if there were substantial inhomogeneities in magnetic field strength along each line of sight, as is expected if the filaments are composed of bundles of fibers (Section 5.3). These inhomogeneities and broader spectra are also expected in the diffuse lobes of 3C40B (see Section A and Figure 12, respectively).

The synchrotron spectra would also be broadened if the underlying electron spectra themselves do not cut off exponentially, but fall more gradually at higher energies. Such a stretching of the electron spectrum is naturally expected in the case of stochastic reacceleration because it induces particle diffusion in momentum space (e.g., Brunetti & Jones 2014). In particular, betatron reacceleration to GeV energies of a population of electrons previously maintained at energies of several 100 MeV by ICM turbulence naturally broadens the spectrum, and thus provides a plausible mechanism for illuminating the *E-fils*.

5.6. Filaments and X-Ray Cavities

One of the more striking results from this work is the existence of a channel with extremely low thermal X-ray emitting plasma that overlaps with the *E-fils*. Cavities in the ICM created by radio jets/lobes have been extensively studied (e.g., Hlavacek-Larrondo et al. 2015, and references therein) and the PdV work needed to create them appears to be consistent with the kinetic luminosity of the radio jets (Bîrzan et al. 2004). The southern lobe of 3C40B is another example of a cavity that may have been driven by such jet flows (Bogdan et al. 2011).

The *E-fils* are perpendicular to the 3C40B jet flow, so it is unlikely that a bulk flow from the AGN has dumped its energy along the *E-fils* path and created a cavity. In addition, a cavity produced in this way would quickly refill this relatively narrow (35 kpc) low-density region. Shear motions in the ICM do not themselves create cavities in the medium; however, by amplifying magnetic fields, accompanied by cosmic-ray acceleration, they can build up pressures that could be comparable to those in the thermal ICM, and thus plausibly exclude the thermal plasma. In A194, Bogdan et al. (2011) suggest that NGC 541 and NGC 545 are falling through the cluster center associated with NGC 547. The direction of motion is thus W to E, in the same general direction as the *E-fils*, lending support to this picture.

A similar X-ray faint channel was found in A520 by Wang et al. (2016; see their Figure 5). It is observed to be 30 kpc wide and 200 kpc long, very similar to that associated with the *E-fils*. They found, similar to A194, that the observed size of the cavity would not produce a strong enough dip in the X-rays, and assume a much broader evacuated region. (We assumed a flattened thermal medium, instead.) They also suggest that magnetic fields, enhanced in a minor merger along the direction of the cavity, reached pressures where they could exclude the thermal plasma. In A520, the channel is embedded in extended radio halo-type emission (Hoang et al. 2019), but no radio

emission specifically associated with the channel can be recognized.

These observations indicate that shear-amplified magnetic fields can produce X-ray cavities. It is therefore appropriate to ask whether the buildup of magnetic (and perhaps accompanying cosmic ray) pressure is also important for cavities associated with radio lobes, such as the southern lobe of 3C40B. Our Faraday results show that the nonthermal synchrotron emissions within the southern lobe are filamentary and intertwined with thermal plasma, because different filaments show different Faraday depths. As discussed by Bell et al. (2019), radio galaxy lobes represent cavities formed by AGN plasma backflowing from the jet head within an ambient thermal plasma. Inside these lobes, high-pressure magnetic flux tubes form intermittently throughout the volume and can accelerate cosmic rays to high energies. Thus, the relative roles of bulk and magnetic pressure in creating X-ray cavities is worth further investigation.

6. Concluding Remarks

In Section 3 we summarized our observational findings on the A194 system. The extensive network of radio filaments, and especially the prominent *E-fils*, illuminate the evolving MHD properties of the ICM and the accompanying acceleration of cosmic rays. They add to the rapidly rising number of filamentary systems seen in clusters and presented the first opportunity to derive some physical parameters based on their interaction with a jet flow.

The combination of many factors allowed us to detect and study the *E-fils*. These included observational factors, such as the low redshift of A194, combined with the high resolution of MeerKAT (and LOFAR), combined with excellent sensitivity and dynamic range. Special opportunities were created by A194's low mass and lack of small-scale strong Faraday depth fluctuations, combined with the likely large-scale motions from the ongoing merger activity.

The analyses presented here allow us to draw more general conclusions regarding the nature of the ICM and its interactions with the relativistic plasma. These include:

1. Magnetized filamentary structures, often or always in bundles, are a natural consequence of high-β MHD flows in the lobes of radio galaxies and in the surrounding thermal medium.
2. The lengths of filaments are an important indicator of the dominant physical scales in the kinematics of the plasmas; the widths of the filaments are an important indicator of the physics/microphysics regulating their origin and evolution.
3. Magnetic fields in the filaments can be stretched and amplified by interactions by flows in the ICM and radio galaxies to levels where the magnetic pressure reflects the stresses in the ICM flows ($\rho v^2/\ell$, where ρ is the density of the turbulent plasma, with a characteristic velocity v on the driving scale ℓ). This is comparable to the thermal pressure ($\beta \sim 1$), so magnetic filaments can form X-ray cavities.
4. Magnetic filaments embedded in cluster turbulence are an additional site where CRe can be reaccelerated, e.g., out of a minimum-maintenance pool of several 100MeV electrons.

5. Where the foreground fluctuations are small in Faraday depth, the observed Faraday depths to filaments and jets permit characterization of their 3D structures.
6. Inside the lobes of radio galaxies, filamentary synchrotron-emitting structures appear to be intertwined with and thus have comparable pressures to the surrounding thermal plasma.

These findings point the way to important opportunities for further study. For 3D Faraday structure mapping, studies of other radio galaxies in groups or other situations where only minor small-scale Faraday depth fluctuations are present would be important. Additional examples where filament structures had been perturbed by their interactions with AGN outflows could test the ideas presented here, in particular the roles of magnetic field amplification via stretching. Multifrequency studies of the spectral structures of filaments and possible variations as a function of position from potential cosmic-ray sources are needed to probe the acceleration histories. Prospects for much higher-resolution studies of filaments to characterize their substructures are challenging, but essential.

Appendix A
A194 Filament System

The filaments discussed in this paper (*E-fils*) are the brightest of an extensive network of filaments both interior to the lobes of 3C40B and elsewhere in the ICM, especially in the region between 3C40B and the extended linear twin structures to the north of 3C40A, as shown in Figure 24. Their analysis is beyond the scope of the current paper, but would certainly contribute to a more complete understanding of filament origins and properties.

One major question is whether filaments represent minor enhancements in emissivity above the more diffuse surrounding emission, or whether they illuminate a highly intermittent magnetized plasma with large variations in emissivity. To provide some quantitative information on this issue, we measured the rms fluctuations in an $\sim310'' \times 240''$ box in the far northern lobe of 3C40B (in the original unfiltered $7\rlap{.}''75$ map), and compared this to the mean brightness. The rms was $70\,\mu$Jy beam^{-1} and the mean was $460\,\mu$Jy beam^{-1}, respectively, or $\sim15\%$. If the filaments are cylindrical, then the line of sight through them is ~5–$10\times$less than that of the more diffuse lobe. They thus represent changes in emissivity of order unity; they are not minor enhancements. The bright southern lobe associated with the X-ray has corresponding values of 1.4 mJy beam^{-1} rms and 5.3 mJy beam^{-1} mean, or $\sim25\%$, with similar implications. The enhancements in emissivity are even more pronounced in the filaments in the far southern lobe and the region between 3C40B and 3C40A; the corresponding rms (mean), percent, and [box size] values are 140(280) μJy beam^{-1}, $\sim50\%,[250'' \times 250'']$ and 90(220) μJy beam^{-1}, $\sim40\%,[275'' \times 100'']$, respectively.
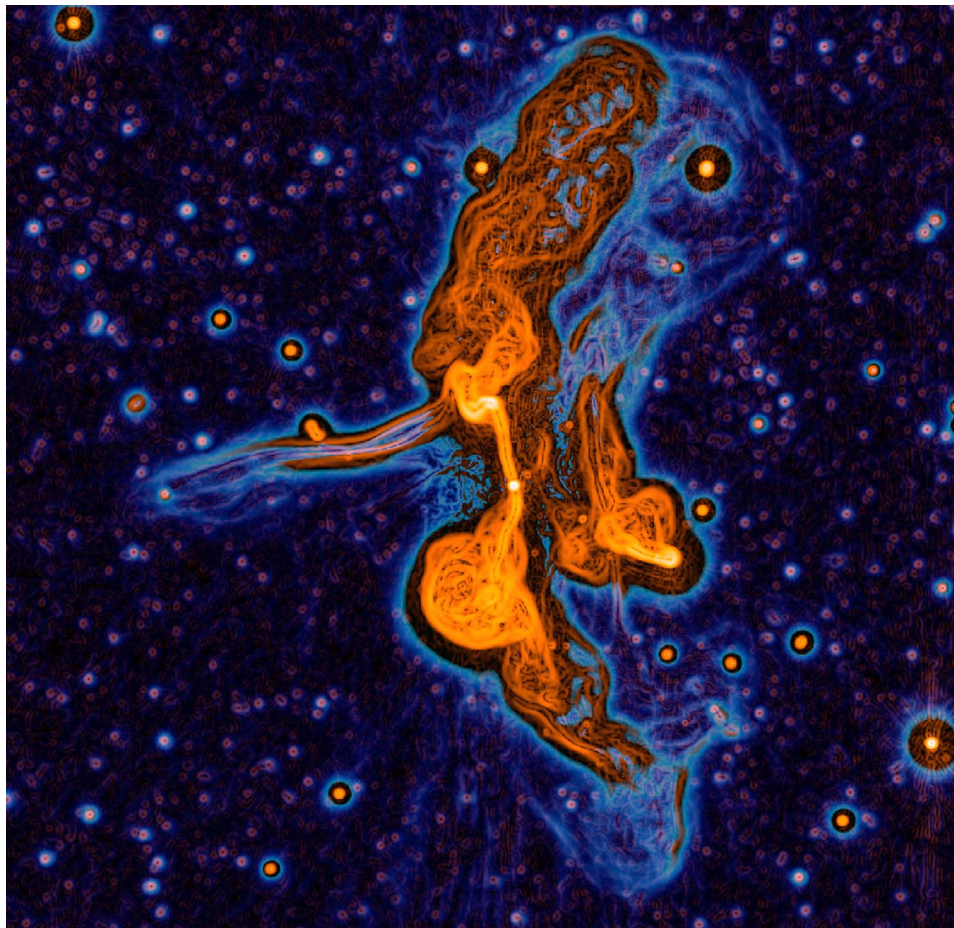

Figure 24. Filtered $7\rlap{.}''75$ image of A194 to emphasize the filamentary structures inside and outside of the radio galaxy lobes. In orange we show the results from a Sobel edge-detection filter (NINER task in AIPS), and in blue we show the results from Gaussian gradient magnitude filtering (Walker et al. 2016).

Appendix B
Explorations in 3D

In this paper, we have inferred the 3D structure of various features using their Faraday depths. This appears to be a very promising diagnostic tool under the right conditions. Here we explore the major assumptions and caveats behind the 3D analysis.

A194 presents an unusual opportunity by virtue of its very small scatter in Faraday depth (Govoni et al. 2017, and as observed here, ∼10 rad m^{-2}). In more massive clusters, the typical scatter in RM values is much larger—e.g., ∼150 rad/m^2 near the center of A2345 (Stuardi et al. 2021) and 303 and 166 rad m^{-2} for the Coma cluster central galaxies (Bonafede et al. 2010). The mean RM for A194 is also consistent with the Milky Way foreground (Figure 5), implying no detectable net contribution from the cluster. We also measured the RMs at the peaks of 21 components from background and possible cluster sources where the polarized intensity was >100 μJy beam^{-1}. The net mean (rms scatter) for these polarized components were 5.7 (8.3 rad m^{-2}). The low-mass A194 system is thus currently unique among clusters with Faraday studies, where the foreground contributions to the RM are small. Random foreground variations in RM, e.g., are very unlikely to produce distinct RM structures right where the northern jet of 3C40B undergoes multiple bends (Figure 4, bottom right) compared to the adjacent *E-fils* and diffuse lobes. Similarly, in the southern lobe, different filamentary structures have different RMs, which is unlikely to arise with random foreground patches. One simple interpretation of the RM variations, then, is that they represent the depth to each structure in the embedding thermal medium.

The question remains about how to translate between physical depth and Faraday depth. The Faraday depth is ∝ $B\,n_e\,dl$, where B is the (signed) component of the magnetic field along the line of sight, n_e is the local electron density, and dl is the incremental path length. Because of the sign ambiguity, an increasing Faraday depth in a given location could be due to a structure being farther away from us with a local field pointing away from us, or to a structure being closer to us with a local field pointing toward us. If the overall structure has Faraday depths that scatter around the Milky Way value, as is true for A194 (see Figure 5), then there is no net large-scale field to resolve the sign ambiguity. The continuity of Faraday depths as a function of position (as seen in multiple figures here) suggests that for large regions, the sign stays constant while the line-of-sight depth changes. For determining 3D structures, changes in the strength of B and the local density n_e will also change the scaling of physical depth with Faraday depth. At present, there is no way to separate out these variations on small scales; on larger scales, e.g., 100 s of kpc, some constraints might be available from X-ray modeling of the density, coupled with assumptions about how the magnetic field scales with density.

In Figure 16 we show the Faraday depth along the the *E-fils* together with the sky view. There is a general, but not perfect, correspondence between bends in the jet seen in the plane of the sky and reversals of direction in the magnitude of the Faraday depth along the path. The simplest explanation is that the jet is underdoing bending in 3D. With a large enough sample of bends and excursions, we could make the assumption that the plane of the sky is not a privileged direction and that the bends are of similar magnitude in all three
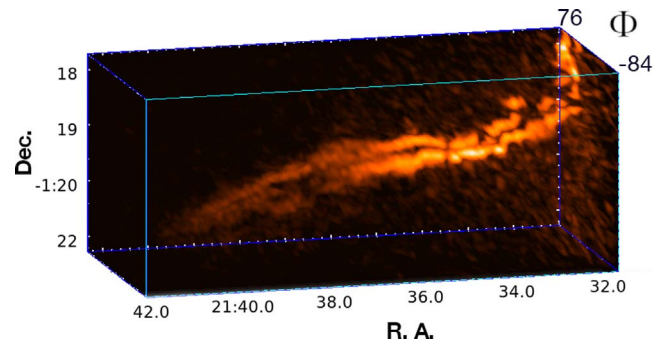

Figure 25. Polarized intensity snapshot of the *E-fils* at a rotation of 30° in the RA/Dec/Φ cube. All three axes are labeled. Each pixel in the image shows the maximum brightness along that line of sight in the projected/rotated cube. An animated version of this figure is available in the HTML version. The animation is 12 seconds long and rotates around the decl. axis, starting with an orientation in the plane of the sky (0°), then rotating 180° to view the source from behind, and then returning to 0°. Midway through the rotation, at 90°, the view is in the decl. (vertical) versus ϕ (horizontal) plane, effectively a side view of the structure. The animation does not have axis labels.
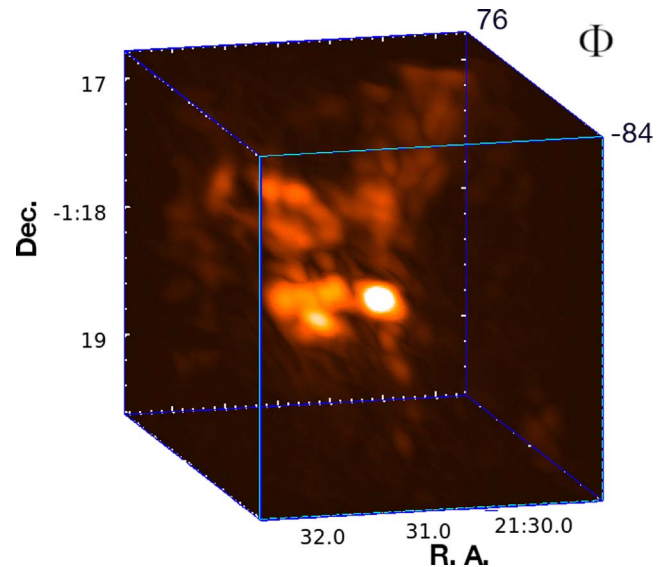
(An animation of this figure is available.)

Figure 26. Polarized intensity snapshot of the region around the bends in the north jet of 3C40B. See the detailed description of the accompanying animation in the caption of Figure 25.

(An animation of this figure is available.)

dimensions. With this assumption, we could ask which magnitude of the magnetic field was present in the surrounding medium. We illustrate this exercise using a local density of ∼10^{-3} cm^{-3} derived from the X-rays, a distance between bends of ∼15 kpc, the Faraday depth (ϕ), and variations between reversals of ∼30 rad m^{-2}. This yields B(μG) = $\phi\,[0.8\,n_e(\text{cm}^{-3})\,dl\,(\text{pc})]^{-1}$ ∼ 2.5 μG, similar to the value of ∼1.4 μG derived in Section 4.6.

As an exploratory tool, we now assume a constant scaling of physical depth with Faraday depth, with no sign changes, and present four movies of selected regions linked to Figures 25, 26, 27 and 28 *(see the files named in the caption)*. For visualization purposes, we adopt a somewhat arbitrary scaling of 0.56 rad m^{-2} = 1″, which yields curvatures in structures along the line of sight similar to curvatures in the plane of the sky for the northern jet. Note that there is a front-back
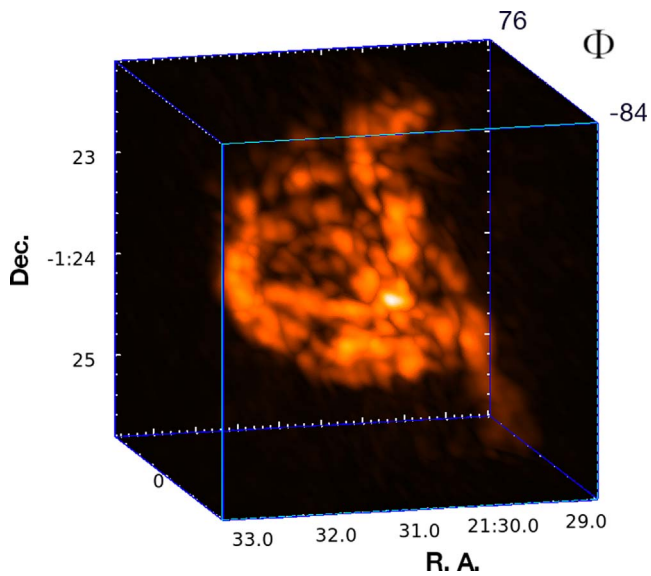
Figure 27. Polarized intensity snapshot of the southern lobe of 3C40B. See the detailed description of the accompanying animation in the caption of Figure 25.

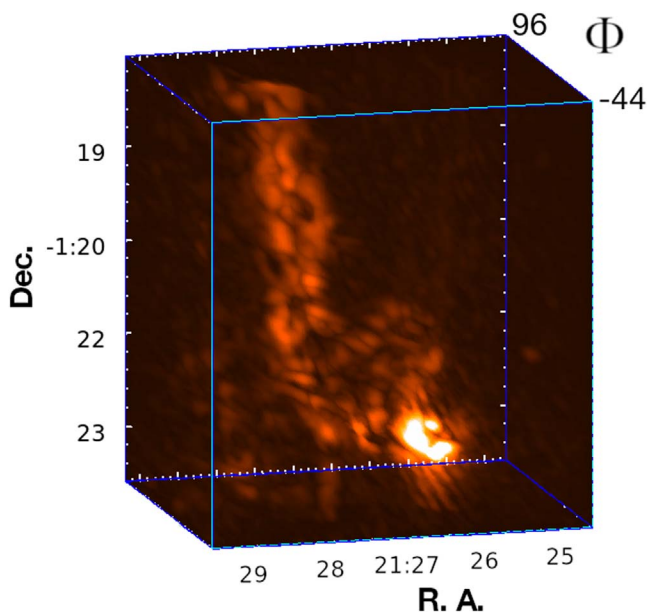(An animation of this figure is available.)

Figure 28. Polarized intensity snapshot of 3C40A. See the detailed description of the accompanying animation in the caption of Figure 25.

(An animation of this figure is available.)

ambiguity, corresponding to the unknown sign of the magnetic field along the line of sight.

In the *E-fils* movie, (Figure 25) the filaments curve along the line of sight as they approach the right edge (where they meet 3C40B's northern jet), exactly where they wrap around the jet in the plane of the sky (Figure 19). In the northern jet movie (Figure 26), the bends along the line of sight occur where bends are seen in the plane of the sky. At the bright spot (point A in Figure 20), the structure is broadened in Faraday depth space, suggesting a dense thermal region at the bend. The southern lobe looks flattened (Figure 27), perhaps because the densities there are actually lower than in the assumed scaling. Similarly, the *E-fils* are likely in lower-density regions than the jets, and

could be more curved along the line of sight than shown here. We include a movie of 3C40A that 3C40A (Figure 28), that is not otherwise discussed in this paper. The pair of filaments extended north from the radio galaxy appear to twist around each other, as is also suggested by the apparent braiding of the Faraday-depth-colored structures in Figure 4.

ORCID iDs

L. Rudnick ⓘ https://orcid.org/0000-0001-5636-7213
M. Brüggen ⓘ https://orcid.org/0000-0002-3369-7735
G. Brunetti ⓘ https://orcid.org/0000-0003-4195-8613
W. D. Cotton ⓘ https://orcid.org/0000-0001-7363-6489
W. Forman ⓘ https://orcid.org/0000-0002-9478-1682
T. W. Jones ⓘ https://orcid.org/0000-0002-9368-4418
C. Nolting ⓘ https://orcid.org/0000-0002-0775-6017
G. Schellenberger ⓘ https://orcid.org/0000-0002-4962-0740
R. van Weeren ⓘ https://orcid.org/0000-0002-0587-1660

References

Abell, G. O., Corwin, H. G., & Olowin, R. P. 1989, ApJS, 70, 1
Alam, S., Albareti, F. D., Allende Prieto, C., et al. 2015, ApJS, 219, 12
Bell, A. R., Matthews, J. H., Blundell, K. M., & Araudo, A. T. 2019, MNRAS, 487, 4571
Bîrzan, L., Rafferty, D. A., McNamara, B. R., Wise, M. W., & Nulsen, P. E. J. 2004, ApJ, 607, 800
Bogdan, A., Kraft, R. P., Forman, W. R., et al. 2011, ApJ, 743, 59
Bonafede, A., Feretti, L., Murgia, M., et al. 2010, A&A, 513, A30
Botteon, A., Brunetti, G., van Weeren, R. J., et al. 2020, ApJ, 897, 93
Brentjens, M. A., & de Bruyn, A. G. 2005, A&A, 441, 1217
Brienza, M., Lovisari, L., Rajpurohit, K., et al. 2022, A&A, 661, A92
Brodie, J. P., Bowyer, S., & McCarthy, P. 1985, ApJL, 293, L59
Brunetti, G., Setti, G., & Comastri, A. 1997, A&A, 325, 898
Brunetti, G., & Jones, T. W. 2014, IJMPD, 23, 1430007
Camilo, F., Scholz, P., Serylak, M., et al. 2018, ApJ, 856, 180
Churazov, E., Forman, W., Jones, C., & Böhringer, H. 2000, A&A, 356, 788
Churazov, E., Vikhlinin, A., Zhuravleva, I., et al. 2012, MNRAS, 421, 1123
Condon, J. J., Cotton, W. D., White, S. V., et al. 2021, ApJ, 917, 18
Cotton, W. D. 2008, PASP, 120, 439
Cotton, W., Condon, J., Kellermann, K., et al. 2018, ApJ, 856, 67
Croft, S., van Breugel, W., de Vries, W., et al. 2006, ApJ, 647, 1040
de Gasperin, F., Intema, H. T., Shimwell, T. W., et al. 2017, SciA, 3, e1701634
de Gasperin, F., Dijkema, T. J., Drabent, A., et al. 2019, A&A, 622, A5
de Gasperin, F., Rudnick, L., Finoguenov, A., et al. 2022, A&A, 659, A146
Ekers, R. D., Fanti, R., Lari, C., & Parma, P. 1978, Natur, 276, 588
Fabian, A. C. 2012, ARA&A, 50, 455
Galishnikova, A. K., Kunz, M. W., & Schekochihin, A. A. 2022, arXiv:2201.07757
Gendron-Marsolais, M.-L., Hull, C. L. H., Perley, R., et al. 2021, ApJ, 911, 56
Govoni, F., Murgia, M., Feretti, L., et al. 2005, A&A, 430, L5
Govoni, F., Murgia, M., Vacca, V., et al. 2017, A&A, 603, A122
Guidetti, D., Laing, R. A., Bridle, A. H., Parma, P., & Gregorini, L. 2011, MNRAS, 413, 2525
Guidetti, D., Laing, R. A., Croston, J. H., Bridle, A. H., & Parma, P. 2012, MNRAS, 423, 1335
Jetha, N. N., Hardcastle, M. J., & Sakelliou, I. 2006, MNRAS, 368, 609
Hines, D. C., Owen, F. N., & Eilek, J. A. 1989, ApJ, 347, 713
Hlavacek-Larrondo, J., McDonald, M., Benson, B. A., et al. 2015, ApJ, 805, 35
Hoang, D. N., Shimwell, T. W., van Weeren, R. J., et al. 2019, A&A, 622, A20
Hu, H., Qiu, Y., Gendron-Marsolais, M.-L., et al. 2022, ApJL, 929, L30
Hudaverdi, M., Kunieda, H., Tanaka, T., et al. 2006, PASJ, 58, 931
Jaffe, W. J., & Perola, G. C. 1973, A&A, 26, 423
Jonas, J. & MeerKAT Team 2016, in MeerKAT Science: On the Pathway to the SKA (Trieste: SISSA), 1
Katz-Stone, D. M., Rudnick, L., & Anderson, M. C. 1993, ApJ, 407, 549
Katz-Stone, D. M., & Rudnick, L. 1997, ApJ, 479, 258
Knowles, K., Cotton, W. D., Rudnick, L., et al. 2022, A&A, 657, A56
Lame'e, M. M. 2017, PhD Thesis, Univ. Minnesota
Lazarian, A., & Vishniac, E. T. 1999, ApJ, 517, 700
Lazarian, A., & Xu, S. 2021, ApJ, 923, 53
Lovisari, L., Reiprich, T. H., & Schellenberger, G. 2015, A&A, 573, A118
Lupton, R. H., & Gott, J. R. 1982, ApJ, 255, 408

Mandal, S., Intema, H. T., van Weeren, R. J., et al. 2020, A&A, 634, A4
Mahdavi, A., Finoguenov, A., Böhringer, H., Geller, M. J., & Henry, J. P. 2005, ApJ, 622, 187
Markevitch, M., & Vikhlinin, A. 2007, PhR, 443, 1
McNamara, B. R., Wise, M., Nulsen, P. E. J., et al. 2000, ApJL, 534, L135
Melrose, D. B. 1980, Plasma astrohysics. Nonthermal processes in diffuse magnetized plasmas - Vol.1: The emission, absorption and transfer of waves in plasmas; Vol.2: Astrophysical applications (New York: Gordon and Breach), 1980
Milne, D. K. 1995, MNRAS, 277, 1435
Miniati, F., & Beresnyak, A. 2015, Natur, 523, 59
Müller, A., Pfrommer, C., Ignesti, A., et al. 2021, MNRAS, 508, 5326
Müller, A., Poggianti, B. M., Pfrommer, C., et al. 2021, NatAs, 5, 159
Murgia, M., Govoni, F., Feretti, L., et al. 2004, A&A, 424, 429
Nagai, D., Lau, E. T., Avestruz, C., Nelson, K., & Rudd, D. H. 2013, ApJ, 777, 137
Nolting, C., Jones, T. W., O'Neill, B. J., & Mendygral, P. J. 2019, ApJ, 876, 154
Nolting, C., Lacy, M., Croft, S., et al. 2022, arXiv:2206.04757
O'Dea, C. P., & Owen, F. N. 1985, AJ, 90, 927
Offringa, A. R., McKinley, B., Hurley-Walker, N., et al. 2014, MNRAS, 444, 606
Offringa, A. R., & Smirnov, O. 2017, MNRAS, 471, 301
Offringa, A. R., van de Gronde, J. J., & Roerdink, J. B. T. M. 2012, A&A, 539, A95
Owen, F. N., Rudnick, L., Eilek, J., et al. 2014, ApJ, 794, 24
Perley, R. A., & Butler, B. J. 2013, ApJS, 206, 16
Pizzo, R. F., de Bruyn, A. G., Bernardi, G., & Brentjens, M. A. 2011, A&A, 525, A104
Porter, D. H., Jones, T. W., & Ryu, D. 2015, ApJ, 810, 93
Rajpurohit, K., Hoeft, M., Wittor, D., et al. 2022a, A&A, 657, A2
Rajpurohit, K., van Weeren, R. J., Hoeft, M., et al. 2022b, ApJ, 927, 80
Ramatsoku, M., Murgia, M., Vacca, V., et al. 2020, A&A, 636, L1
Rines, K., Geller, M. J., Diaferio, A., & Kurtz, M. J. 2013, ApJ, 767, 15
Rudnick, L. 2002, PASP, 114, 427
Rudnick, L. 2019, arXiv:1901.09448
Rudnick, L., & Blundell, K. M. 2003, ApJ, 588, 143
Sakelliou, I., Hardcastle, M. J., & Jetha, N. N. 2008, MNRAS, 384, 87
Sanders, J. S., & Fabian, A. C. 2007, MNRAS, 381, 1381
Sarazin, C. L. 1999, ApJ, 520, 529
Schekochihin, A. A., & Cowley, S. C. 2007, Magnetohydrodynamics: Historical Evolution and Trends, Vol. 85 (Dordrecht: Springer), 85

Stroe, A., Harwood, J. J., Hardcastle, M. J., & Röttgering, H. J. A. 2014, MNRAS, 445, 1213
Shimwell, T. W., Röttgering, H. J. A., Best, P. N., et al. 2017, A&A, 598, A104
Shimwell, T. W., Tasse, C., Hardcastle, M. J., et al. 2019, A&A, 622, A1
Shimwell, T. W., Hardcastle, M. J., Tasse, C., et al. 2022, A&A, 659, A1
Snowden, S. L., Mushotzky, R. F., Kuntz, K. D., & Davis, D. S. 2008, A&A, 478, 615
Stuardi, C., Bonafede, A., Lovisari, L., et al. 2021, MNRAS, 502, 2518
Šuhada, R., Fassbender, R., Nastasi, A., et al. 2011, A&A, 530, A110
Struble, M. F., & Rood, H. J. 1999, ApJS, 125, 35
Tasse, C., Shimwell, T., Hardcastle, M. J., et al. 2021, A&A, 648, A1
Tasse, C. 2014, A&A, 566, A127
Tasse, C., Hugo, B., Mirmont, M., et al. 2018, A&A, 611, A87
van Breugel, W., Filippenko, A. V., Heckman, T., & Miley, G. 1985, ApJ, 293, 83
van Haarlem, M. P., Wise, M. W., Gunst, A. W., et al. 2013, A&A, 556, A2
van Weeren, R. J., de Gasperin, F., Akamatsu, H., et al. 2019, SSRv, 215, 16
van Weeren, R. J., Shimwell, T. W., Botteon, A., et al. 2021, A&A, 651, A115
Vazza, F., Tormen, G., Cassano, R., Brunetti, G., & Dolag, K. 2006, MNRAS Lett., 369, L14
Vazza, F., Angelinelli, M., Jones, T. W., et al. 2018, MNRAS Lett., 481, L120
Vazza, F., Brunetti, G., Brüggen, M., & Bonafede, A. 2018, MNRAS, 474, 1672
Venturi, T., Giacintucci, S., Merluzzi, P., et al. 2022, A&A, 660, A81
Walker, S. A., Sanders, J. S., & Fabian, A. C. 2016, MNRAS, 461, 684
Wang, Q. H. S., Markevitch, M., & Giacintucci, S. 2016, ApJ, 833, 99
Wilber, A., Brüggen, M., Bonafede, A., et al. 2018, MNRAS, 476, 3415
Williams, W. L., van Weeren, R. J., Röttgering, H. J. A., et al. 2016, MNRAS, 460, 2385
Wykes, S., Intema, H. T., Hardcastle, M. J., et al. 2014, MNRAS, 442, 2867
Xu, S., & Lazarian, A. 2022, ApJ, 927, 94
Yusef-Zadeh, F., Wardle, M., Heinke, C., et al. 2021, MNRAS, 500, 3142
Zhang, C., Churazov, E., Forman, W. R., & Lyskova, N. 2019, MNRAS, 488, 5259
ZuHone, J. A., Markevitch, M., Weinberger, R., Nulsen, P., & Ehlert, K. 2021, ApJ, 914, 73
ZuHone, J., Ehlert, K., Weinberger, R., & Pfrommer, C. 2021, Galax, 9, 91
Zhuravleva, I., Churazov, E., Arévalo, P., et al. 2016, MNRAS, 458, 2902
Zhuravleva, I., Churazov, E., Schekochihin, A. A., et al. 2014, Natur, 515, 85
Zhuravleva, I., Churazov, E., Schekochihin, A. A., et al. 2019, NatAs, 3, 832